

2015-07-24

# Water Wave Green's Function Retrieval from a Random Wave Field

Chuntao Lu

*University of Miami*, lufei1987@gmail.com

Follow this and additional works at: [https://scholarlyrepository.miami.edu/oa\\_dissertations](https://scholarlyrepository.miami.edu/oa_dissertations)

---

## Recommended Citation

Lu, Chuntao, "Water Wave Green's Function Retrieval from a Random Wave Field" (2015). *Open Access Dissertations*. 1488.  
[https://scholarlyrepository.miami.edu/oa\\_dissertations/1488](https://scholarlyrepository.miami.edu/oa_dissertations/1488)

This Open access is brought to you for free and open access by the Electronic Theses and Dissertations at Scholarly Repository. It has been accepted for inclusion in Open Access Dissertations by an authorized administrator of Scholarly Repository. For more information, please contact [repository.library@miami.edu](mailto:repository.library@miami.edu).

UNIVERSITY OF MIAMI

WATER WAVE GREEN'S FUNCTION RETRIEVAL FROM A RANDOM WAVE  
FIELD

By

Chuntao Lu

A DISSERTATION

Submitted to the Faculty  
of the University of Miami  
in partial fulfillment of the requirements for  
the degree of Doctor of Philosophy

Coral Gables, Florida

August 2015

©2015  
Chuntao Lu  
All Rights Reserved

UNIVERSITY OF MIAMI

A dissertation submitted in partial fulfillment of  
the requirements for the degree of  
Doctor of Philosophy

WATER WAVE GREEN'S FUNCTION RETRIEVAL FROM A RANDOM WAVE  
FIELD

Chuntao Lu

Approved:

\_\_\_\_\_  
Michael G. Brown, Ph.D.  
Professor of Applied Marine Physics

\_\_\_\_\_  
Roland Romeiser, Dr.rer.nat  
Associate Professor of Applied  
Marine Physics

\_\_\_\_\_  
Jorge F. Willemsen, Ph.D.  
Professor of Applied Marine Physics

\_\_\_\_\_  
Dean of the Graduate School

\_\_\_\_\_  
Guoqing Lin, Ph.D.  
Associate Professor of Marine Geology and Geophysics

LU, CHUNTAO

(Ph.D., Applied Marine Physics)

Water Wave Green's Function Retrieval from  
A Random Wave Field

(August 2015)

Abstract of a dissertation at the University of Miami.

Dissertation supervised by Professor Michael G. Brown.

No. of pages in text. (90)

It has recently been shown that the Green's function in a wave field, which describes deterministic wave propagation from one location to another, can be retrieved by cross-correlating records of random waves measured at those two locations. This simple yet powerful approach, usually called random wave interferometry, has been successfully demonstrated in many different wave fields. This dissertation aims to explore the applicability of random surface gravity wave interferometry in a water wave field. Previous research, especially in ocean acoustics and seismology, is reviewed for better understanding of the theory and practice. Theoretical derivations of the basic result underlying water wave interferometry in both open and closed systems are presented. Following the specifications described in derivations, numerical simulations are performed in open and closed environments; these yield good agreement with theoretical predictions. A wave tank experiment is designed and conducted based on the closed system simulation; the Green's function retrieval in this experiment is also successful. Surface wave elevation data collected during two past major field experiments is analyzed using the random wave interferometry technique. However, results from these field experiment data are not as consistent with theoretical predictions. Possible reasons are discussed.

# Acknowledgements

I would like to thank my advisor, Dr. Michael G. Brown, for his unwavering support and encouragement over the years. I am deeply grateful for his patience and caring, without his excellent guidance and persistent help this dissertation would not have been possible.

I also want to thank my committee members Jorge F. Willemsen, Roland Romeiser and Guoqing Lin for their guidance and insightful feedback with my research work.

I would like to thank Hans C. Graber, Rafael Ramos and William M. Drennan for sharing their field experiments measurements, without which my research work would have been incomplete.

I also like to thank Brian Haus for the opportunity to perform experiments in the wave tank. I can't thank more to Nathan Laxague and Dave Ortiz-Suslow who helped tremendously on conducting the experiments and preprocessing the measurements.

I would like to thank all the kind people here at RSMAS who together provided a wonderful experience for me during the last 5 years, it has truly been an incredible journey.

Finally I like to thank my family and friends for their unconditional support and love.

# Contents

<b>List of Figures</b>	<b>vi</b>
<b>1 Introduction</b>	<b>1</b>
1.1 Green's function primer . . . . .	1
1.2 Green's function retrieval . . . . .	3
1.3 Thesis organization . . . . .	5
<b>2 Literature Review</b>	<b>7</b>
2.1 Conjecture proved . . . . .	7
2.2 Focused Study . . . . .	11
2.2.1 Ocean acoustics . . . . .	12
2.2.2 Seismology . . . . .	16
<b>3 Theoretical Derivations</b>	<b>20</b>
3.1 Preliminaries . . . . .	20
3.2 General derivation . . . . .	24
3.3 Closed system derivation . . . . .	29

<b>4</b>	<b>Numerical Simulations</b>	<b>34</b>
4.1	Open system simulation . . . . .	36
4.2	Closed system simulation . . . . .	43
<b>5</b>	<b>Field Experiment Data Analysis</b>	<b>52</b>
5.1	FETCH experiment . . . . .	53
5.2	SW06 experiment . . . . .	59
<b>6</b>	<b>Wave Tank Experiment</b>	<b>65</b>
6.1	The wave tank facility . . . . .	66
6.2	Experiment procedure . . . . .	67
6.3	Data analysis . . . . .	73
<b>7</b>	<b>Conclusion and Discussion</b>	<b>80</b>
	<b>Bibliography</b>	<b>85</b>

# List of Figures

- 2.1 Lobkis and Weaver’s ultrasonic experiment configuration. On the surface of an irregular shaped aluminum block, a transient pulse is generated at  $s$  and the corresponding wave field is measured at  $x_x$  and  $x_y$ . Adapted from ”On the emergence of the Greens function in the correlations of a diffuse field” by Lobkis, Oleg I. and Weaver, Richard L. *The Journal of the Acoustical Society of America*, 110(6):3011,2001. . . . . 11
- 2.2 Acoustic channels used in Roux and Fink’s numerical simulation. (a) is for range-independent case where water depth is 100 m and  $B$  is 40 m from the surface; (b) is for range-dependent case where water depth changes from 100 m to 50 m and then back to 100 m from left to right, and  $B$  is at the same water depth as in (a). Adapted from ”Greens function estimation using secondary sources in a shallow water environment” by Roux, Philippe and Fink, Mathias. *The Journal of the Acoustical Society of America*, 113(3):1406, 2003. . . . . 15

4.1	100000 sources (blue dots) are randomly distributed in a circular region whose radius is 500 m. Two receivers $A$ and $B$ (red dots) are centered around the origin and 100 m away from each other. . . . .	37
4.2	Simulated time series of surface elevation (40960 s) at $A$ (upper panel) and $B$ (lower panel), amplitude units are arbitrary. For viewing purpose, a few measurements with numeric values bigger than 20 are truncated in the plot.	41
4.3	Surface elevation response $d(t) * G_\eta(\mathbf{x}_B \mathbf{x}_A, t)$ at $B$ due to single point source impulsive excitation at $A$ in the open system. The elevation is normalized to have a maximum value of 1. . . . .	42
4.4	Cross-correlation $C_{AB}(t)$ (red dashed curve) of surface elevations $\eta(\mathbf{x}_A, t)$ and $\eta(\mathbf{x}_B, t)$ in the open system with deep water dispersion relation, compared to $D(t) * [G_\eta(\mathbf{x}_B \mathbf{x}_A, t) + G_\eta(\mathbf{x}_B \mathbf{x}_A, -t)]$ (blue curve). The cross-correlation is averaged over 6000 realizations. Both curves are normalized to have maximum value of 1. . . . .	43
4.5	5 hour time series of simulated random surface elevation $\eta(\mathbf{x}_A, t)$ (upper panel) and $\eta(\mathbf{x}_B, t)$ (lower panel) in the wave tank geometry. Both curves are normalized to have a maximum value of 1. . . . .	47
4.6	Simulated surface elevation response $d(t) * G_\eta(\mathbf{x}_B \mathbf{x}_A, t)$ computed based on Eq.3.35 in the wave tank geometry. The curve is normalized to have a maximum value of 1. . . . .	49

4.7 Cross-correlation  $C_{AB}(t)$  (blue curve) of random surface elevation  $\eta(\mathbf{x}_A, t)$  and  $\eta(\mathbf{x}_B, t)$  in the wave tank geometry, compared to  $D(t) * [G_\eta(\mathbf{x}_B|\mathbf{x}_A, t) + G_\eta(\mathbf{x}_B|\mathbf{x}_A, -t)]$ . The cross-correlation is averaged over 240 realizations. Both curves are normalized to have a maximum absolute amplitude of 1. . . . . 50

4.8 Cross-correlation  $(C_{AB}(t) + C_{AB}(-t))/2$  (blue curve) of random surface elevations  $\eta(\mathbf{x}_A, t)$  and  $\eta(\mathbf{x}_B, t)$  in the wave tank geometry, compared to  $D(t) * G_\eta(\mathbf{x}_B|\mathbf{x}_A, t)$ . The cross-correlation is averaged over 240 realizations. Both curves are normalized to have a maximum absolute amplitude of 1. . . . . 51

5.1 Geographic map of the FETCH experiment. Point B is the location of the ASIS buoy from 18 March to 9 April. DWR was also at this location from 16 March to 25 March. Point B' is the location of DWR after 25 March. Adapted from "Directional wave measurements from three wave sensors during the FETCH experiment" by Pettersson, Heidi. *Journal of Geophysical Research*, 108(C3), 2003. . . . . 54

5.2 Wind speed measured by ASIS buoy from March 18 to March 26 during the FETCH experiment. The time period highlighted by the red box has relatively low wind speed and is therefore selected for cross-correlation. The time axis is day in the month of March. . . . . 57

5.3	Surface elevation data measured by DWR (upper panel) and ASIS (lower panel) from 02:20 to 05:00 on March 23. 10 minute gaps appear every 20 minutes in DWR data and 1 minute gaps appear every 29 minutes in ASIS data. ASIS data are resampled and synchronized with the DWR data. The time axis is the total time of the selected data in seconds. . . . .	58
5.4	Cross-correlation $C_{AB}(t)$ of surface elevation $\eta(\mathbf{x}_A, t)$ and $\eta(\mathbf{x}_B, t)$ measured in FETCH experiment. The cross-correlation is averaged over 75 realizations and normalized to have maximum absolute value of 1. . . . .	59
5.5	Geographic map of the ASIS buoys during SW06 experiment. Red circle indicates the location of Romeo and red square indicates the location of Yankee. Adapted from "Determination of internal wave properties from X-Band radar observations" by Ramos, Rafael J., Lund, Björn and Graber, Hans C. <i>Ocean Engineering</i> , 36(14):1039-1047, 2009. . . . .	60
5.6	Wind speed measured by Romeo (blue curve) and Yankee (red curve) from August 2 to August 11 during the SW06 experiment. The time period highlighted by the black box has relatively low wind speed and is therefore selected for cross-correlation. The time axis is the total time in days. . . . .	62
5.7	Surface elevation data measured by Romeo (upper panel) and Yankee (lower panel) from 21:59:00 on August 5, 2006 to 09:11:00 on August 6, 2006. On average 1 minute gaps appear every hour in both Romeo and Yankee data. The time axis is the total time of the selected data in seconds. . . . .	63

5.8	The cross-correlation $C_{AB}(t)$ of surface elevation $\eta(\mathbf{x}_A, t)$ and $\eta(\mathbf{x}_B, t)$ measured in SW06 experiment. The cross-correlation is averaged over 16 realizations and normalized to have maximum absolute value of 1. . . . .	63
5.9	Simulated GF $D(t) * G_\eta(t)$ based on the geometry in SW06 experiment. GF is normalized to have a maximum absolute value of 1. . . . .	64
6.1	A photograph of Air-Sea Interaction Salt water Tank (ASIST). Photograph is taken from the tank head in the along tank direction. Water is not filled in the tank at the time. . . . .	67
6.2	View from inside Air-Sea Interaction Salt water Tank (ASIST). Water in the tank is colored with green dye. . . . .	68
6.3	A schematic of Air-Sea Interaction Salt water Tank (ASIST) . . . . .	70
6.4	A photograph of laser beam in ASIST. A visible water line is brightened by the laser beam which is shot from bottom of the tank. . . . .	71
6.5	5 hour time series of the surface elevation $\eta(\mathbf{x}_A, t)$ (upper panel) and $\eta(\mathbf{x}_B, t)$ (lower panel) measured in the wave tank. Both curves are normalized to have a maximum value of 1. . . . .	73
6.6	Cross-correlation $(C_{AB}(t) + C_{AB}(-t))/2$ (blue curve) of random surface elevations $\eta(\mathbf{x}_A, t)$ and $\eta(\mathbf{x}_B, t)$ measured in the wave tank, compared to $D(t) * G_\eta(\mathbf{x}_B \mathbf{x}_A, t)$ . Cross-correlation is averaged over 240 realizations. Both curves are normalized to have a maximum absolute amplitude of 1. . .	74

6.7 Power spectral density of 5 hour time series of the surface elevation  $\eta(\mathbf{x}_A, t)$  (upper panel) and  $\eta(\mathbf{x}_B, t)$  (lower panel) measured in the wave tank. The spectra are normalized by their maximum values. . . . . 75

6.8 Averaged power density spectrum (blue curve) of 5 hours of time series of the surface elevations  $\eta(\mathbf{x}_A, t)$  and  $\eta(\mathbf{x}_B, t)$ , compared to the weighting function  $\bar{d}(\omega)$  (red curve). Both curves are normalized have a maximum value of 1. . . . . 76

6.9 Theoretical spectrum with empirical weight  $\bar{d}(\omega)|\cos(l\pi x_A/L_x)|$  (red vertical bars) at  $\omega = \omega_l$ , compared to the averaged spectrum  $(|\bar{\eta}(\mathbf{x}_A, \omega)| + |\bar{\eta}(\mathbf{x}_B, \omega)|)/2$  (blue curve) in the wave tank. Both curves are normalized to have a maximum value of 1. . . . . 77

6.10 Cross-correlation  $(C_{AB}(t))$  (blue curve) of random surface elevations  $\eta(\mathbf{x}_A, t)$  and  $\eta(\mathbf{x}_B, t)$  measured in the wave tank, compared to  $D(t) * G_\eta(\mathbf{x}_B|\mathbf{x}_A, t)$  with empirical weight (red curve). The cross-correlation is averaged over 240 realizations. Both curves are normalized to have a maximum absolute value of 1. . . . . 78

6.11 Cross-correlation  $(C_{AB}(t) + C_{AB}(-t))/2$  (blue curve) of random surface elevations  $\eta(\mathbf{x}_A, t)$  and  $\eta(\mathbf{x}_B, t)$  measured in the wave tank, compared to  $D(t) * G_\eta(\mathbf{x}_B|\mathbf{x}_A, t)$  with empirical weight (red curve). The cross-correlation is averaged over 240 realizations. Both curves are normalized to have the same total energy between 3 and 60 s. . . . . 79

# Chapter 1

## Introduction

Background material on the significance of the Green's function (GF) is presented in section 1.1. Basic principles and current state of research relating to Green's function retrieval in various fields as well as the motivation for this thesis work are given in section 1.2. The organization of this thesis is outlined in section 1.3.

### 1.1 Green's function primer

The Green's function was first introduced by and so named in honor of the brilliant English mathematician and physicist George Green(1793-1841)[28]. The GF has been widely studied and explored from the point view of a fundamental solution to a linear differential equation in many areas that involve differential equations. With its unique properties, the GF has been extensively used as a powerful tool to construct useful solutions to differential equations as well as in developing numerical models for solving applied mathematics and

physics problems. The significance of the GF is widely acknowledged in the sense that it is used to solve differential equations arise in all almost branches of engineering and science. While the common application of GF is to solve a differential equation given boundary value conditions on the domain of interest, the exact form of the GF largely depends on the problem domain and varies with the differential equation, boundary conditions and the domain shape. Generally, the advantage of applying GF lies in the fact that using GF gives a solution to the differential equation in the form of an integral. While a direct approach to deal with differential equations via numerical methods often requires approximations to the underlying differential equations as well as the boundary conditions, GF-based procedures mostly don't need to work on any approximations beforehand [28]. Mathematically the GF  $G(x, s, t)$  satisfies

$$LG(x, s, t) = \delta(x - s)\delta(t), \quad (1.1)$$

where  $L$  is a linear differential operator,  $s$  is a point in the domain and  $\delta$  is the Dirac delta function. This is the essential feature that enables GF to solve differential equations which have the form of

$$Lu(x, t) = f(x) \quad (1.2)$$

with a solution as an integral

$$u(x, t) = \int G(x, s, t)f(s)ds. \quad (1.3)$$

## 1.2 Green's function retrieval

From the point view of physics, the GF can be interpreted as the response to a point source excitation in a wave field, which can be used to construct solutions to more general source functions. The GF contains information about physical properties of the environment. Consequently, GF retrieval may be important in applications. It is worth noting that GF is defined in both the frequency domain (response to a time-harmonic source) and the time domain (response to an impulse source). A straightforward solution to GF retrieval is to actively excite impulses at needed locations and record corresponding responses. This approach is theoretically easy to validate and could be feasible when the problem domain has relatively small scale and the operations are not too complicated to perform. However, in reality the procedure will easily become impractical and unaffordable because of the often large domain scale, challenging work involved with impulse excitations and other various domain specific reasons. A less obvious yet practically much more economical way to retrieve the GF is based on the equivalence between GF and cross-correlation of the ambient noise recorded at interested locations in a wave field. Here the concept of ambient noise is by no means confined to the area of acoustics, but should be recognized as a more general description of the random amplitude fluctuations at an arbitrary point in the field. Such fluctuations at a point are the superposition of waves propagating in many different directions, thus are characterized with randomness or noisiness. This methodology of extracting the deterministic GF by processing ambient noise is often known as noise interferometry [52, 11, 62, 57, 43, 48, 6, 24, 58, 61, 47].

Underlying the theory of GF retrieval is the superposition principle, which states the net response at a given place and time caused by multiple sources is the sum of the responses that would have been caused by each individual source. And the superposition principle applies to any linear wave system or environment that is governed by linear equations: hence any generalized GF retrieval approach that is proved to be valid in an arbitrary linear environment has a substantial chance to work in other linear systems or environments. The generalization of GF retrieval, along with its advantage of mere dependence on passive measurements without the need of any investment of active sources, has encouraged great research enthusiasm in many linear wave fields. It has already been widely used by seismologists in extracting seismic surface waves to study the geophysical structure of Earth's crust and mantle [5, 49, 44, 45, 41, 1, 51, 10, 25, 54, 15, 2, 53, 46, 63, 11]. Besides the success in seismology, many researchers also theoretically and experimentally demonstrated the applicability of GF retrieval in various areas such as helioseismology [14, 32, 33], ultrasonics [26, 59, 60], underwater acoustics [7, 34, 35, 36, 42, 17, 18, 50, 56, 8, 4], and atmospheric acoustics [19, 16, 21] etc. One environment that shares very similar dynamics with the above mentioned areas and, has been only briefly explored [20, 22] with the idea of GF retrieval is the water wave field. The main motivation of this thesis work is to more fully understand the techniques of GF retrieval in a water wave field. Although water waves are not be linear waves in a strict sense, the linearized description of the propagation of surface gravity waves with small amplitudes turns to be a rather accurate approximation with regards to the study of wave characteristics and their

effects. With the primary objective of providing both theoretical and experimental proof for feasibility of GF retrieval in a water wave field, this thesis will focus on demonstrating that by cross-correlating time series of apparently random water wave elevations at two arbitrarily different locations we can obtain certain deterministic propagation information of waves generated at one of the locations and measured at the other. Mathematically the fundamental result can be expressed as:

$$\gamma C_{AB}(t) = D(t) * [G_{\eta}(\mathbf{x}_B|\mathbf{x}_A, t) + G_{\eta}(\mathbf{x}_A|\mathbf{x}_B, -t)] \quad (1.4)$$

where  $\gamma$  is a constant,  $C_{AB}(t)$  is the correlation function of surface elevation  $\eta(t)$  at locations  $\mathbf{x}_A$  and  $\mathbf{x}_B$ ,  $D(t)$  is a band-limited approximation to a delta function, and  $G_{\eta}(\mathbf{x}|\mathbf{x}_0, t)$  is the surface elevation GF at location  $\mathbf{x}$  due to point source excitation at  $\mathbf{x}_0$ .

### 1.3 Thesis organization

The overall structure of this thesis is described as follows. Chapter 2 reviews various previous research works in different fields covering from the discovery of GF retrieval to its widespread use in the last decade. Chapter 3 presents the theoretical derivation of GF retrieval via cross-correlation in a water wave field. The derivation leads to the same result in both open and closed systems; it shows the theoretical soundness of GF retrieval with two different types of boundary conditions. Chapter 4 supports the theoretical proof by providing numerical simulations that corresponds to each of the two derivations in

Chapter 3. Chapter 5 gives a detailed analysis of ocean surface elevation data records collected in two field experiments and an attempt to apply the GF retrieval technique as used in numerical simulations. This chapter corresponds to the open system derivation and simulation. Chapter 6 presents an experiment in an indoor rectangular wave tank which is a closed system. Experimental data is processed and compared with the existing numerical result. Chapter 7 is the summary of all the work in this thesis and draws a conclusion based on the findings.

# Chapter 2

## Literature Review

Earlier work on extracting Green's function from random wave cross-correlation in a water wave field is limited to infragravity waves [20, 22]. But there is a substantial amount of research work related to Green's function retrieval by correlating ambient noises in various fields such as acoustics and seismology, where required environment characteristics for applied methodology to work are largely shared by linear water waves. Some of the existing literature on Green's function retrieval by cross correlation is reviewed in this chapter.

### 2.1 Conjecture proved

The fundamental result underlying noise interferometry was first provided by Rytov [39, 40], but this result was unknown to western scientists. Independently, the idea of cross-correlating random noises to extract deterministic wave propagation information has its early validation in the helioseismologic research of Rickett and Claerbout [32].

Their work is based on the conjecture: "By cross-correlating noise traces recorded at two locations on the surface, we can construct the wavefield that would be recorded at one of the locations if there was a source at the other", which was later both theoretically and experimentally proved by Lobkis and Weaver in their ultrasonic research work [26]. While the phase information of a diffuse acoustic field is not predictable due to multiple reflection and scattering, it is coherent and related to features in spectral power densities. Weaver [59] indicated the field's phase has valuable information by relating spectral power densities to local geometry. And Lobkis and Weaver [26] confirmed that the spectrum features in the diffuse field contain explicit information of local responses as they state, "... the temporal cross-correlation function between the signal received simultaneously in two distinct transducers is shown to be the signal which one transducer would receive when the other is given an impulse excitation. The correlation displays all travel paths between the two points, including those with multiple reflections." By assuming all the normal modes in the diffuse field are excited by uncorrelated random noise sources with no particular energy biases, they provide a modal derivation for the relationship between Green's function and cross-correlation in finite systems, which is generally summarized by Snieder and Wapenaar [51] below

In Lobkis and Weaver's derivation, the state of motion, governed by the wave equation  $\frac{\partial^2 v}{\partial t^2} = c^2 \nabla^2 v$ , at location  $\mathbf{x}$  corresponding to the source excitations is given by

$$v(\mathbf{x}, t) = \sum_n (a_n \sin(\omega_n t) + b_n \cos(\omega_n t)) u_n(\mathbf{x}), \quad (2.1)$$

where modal coefficients  $a_n$  and  $b_n$  are random numbers with zero mean and  $\omega_n$  is the angular frequency for mode  $n$ . With the assumption that all normal modes are excited with no energy biases and uncorrelated, the modal coefficients satisfy

$$\langle a_m a_n \rangle = \langle b_m b_n \rangle = S \delta_{mn} \quad \text{and} \quad \langle a_m b_n \rangle = 0, \quad (2.2)$$

where  $\langle \rangle$  denotes ensemble average and  $S$  is the energy of source excitation.

Then the temporal cross-correlation function in the field at two different locations  $\mathbf{x}_A$  and  $\mathbf{x}_B$  is constructed by a time-averaged integration over a finite time interval  $T$ ,

$$C_{AB}(\tau) = \left\langle \frac{1}{T} \int_0^T v(\mathbf{x}_A, t + \tau) v(\mathbf{x}_B, t) dt \right\rangle, \quad (2.3)$$

where  $\tau$  is the time delay in the cross-correlation. After substituting the modal expression of motion in Eq.2.1 into the integral, carrying out the ensemble average and utilizing the properties of modal coefficients in Eq.2.2, the cross-correlation function can be reduced to,

$$C_{AB}(\tau) = S \sum_n u_n(\mathbf{x}_A) u_n(\mathbf{x}_B) \cos(\omega_n \tau). \quad (2.4)$$

The Green's function that describes the wave propagation from  $\mathbf{x}_A$  to  $\mathbf{x}_B$  can be written

$$G(\mathbf{x}_A, \mathbf{x}_B, t) = H(t) \sum_n u_n(\mathbf{x}_A) u_n(\mathbf{x}_B) \cos(\omega_n t) \quad (2.5)$$

where  $H(t)$  is the Heaviside function, zero for negative time and 1 for positive time. A comparison of Eq.2.4 and Eq.2.5 shows that the cross-correlation equals the superposition of the Green's function and its time-reversed counterpart,

$$C_{AB}(\tau) = S[G(x_A, x_B, \tau) + G(x_A, x_B, -\tau)]. \quad (2.6)$$

Lobkis and Weaver also did laboratory work to validate their modal derivation. The experiment is set up using an irregular aluminum block as a closed system, on the surface of which a pulse generating location  $s$  and two response receiving locations  $x_x$  and  $x_y$  were arbitrarily chosen (as shown in Fig.2.1 [26]). A transient pulse generated by an ultrasonic pulser was created at  $s$  and the resulting diffuse field is simultaneously captured at  $x_x$  and  $x_y$  with a two-channel digitizer. The main features of direct pitch-catch signal are successfully found by plotting the cross-correlation of signals received at those two locations; however, many significant amplitude differences were also spotted in the same plot. They managed to improve the quality of the recovered signal by averaging more and increasing the number of sources in the field. Although one can certainly tell the improvements in their plots, unfortunately they did not give any quantitative measurements or analysis with respect to the degree of the similarity between cross-correlation and Green's function.

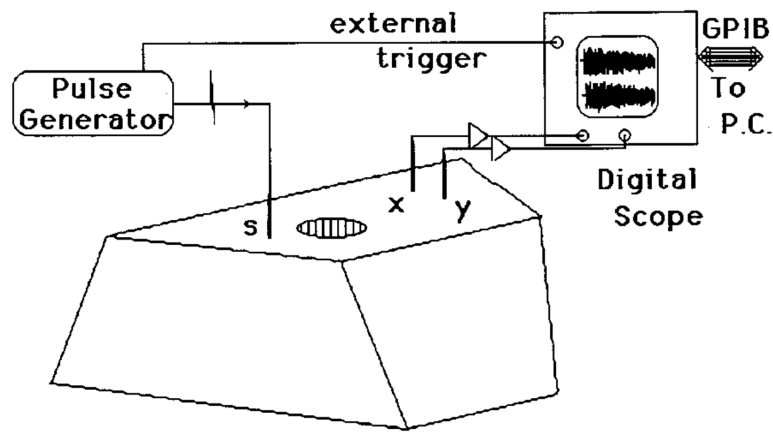


**Figure 2.1:** Lobkis and Weaver’s ultrasonic experiment configuration. On the surface of an irregular shaped aluminum block, a transient pulse is generated at  $s$  and the corresponding wave field is measured at  $x_x$  and  $x_y$ . Adapted from “On the emergence of the Greens function in the correlations of a diffuse field” by Lobkis, Oleg I. and Weaver, Richard L. *The Journal of the Acoustical Society of America*, 110(6):3011,2001.

## 2.2 Focused Study

While Lobkis and Weaver’s remarkable normal-mode derivation is done in the context of closed systems, the same validity for open systems is predicted and considered as promising future research avenue(it turns out that their prediction is indeed correct as they gave the exact proof in a later paper [60]). Lobkis and Weaver named a few potential applications, and many later research efforts in various areas are based on and inspired by their work. Since them, the approach of extracting Green’s function by cross-correlation is most widely studied in ocean acoustics [7, 34, 35, 36, 42, 17] and seismology[5, 49, 44, 45, 41, 1, 51].

### 2.2.1 Ocean acoustics

Roux and Fink [34] studied the same subject in a shallow water environment with an emphasis on its advantage of discretion over traditional time-reversal method in acoustic communication. The time-reversal approach is effective to overcome limitations brought by reverberation and multi-path propagation of acoustic waves in the ocean, but it can not be done without exposing the communicators. It is thus undesirable in the perspective of discrete acoustic communication. Roux and Fink's idea is to introduce secondary sources into the environment so that Green's function between two locations can be obtained by averaging the correlation of received signals. Since both the locations have the single role of receiver (instead of source and receiver in the case of time-reversal) and only relative positions between sources and receivers are required, discrete acoustic communication is achieved. In the theoretical derivation, the environment is set up in two different configurations by varying the position of secondary sources  $S$  relative to receivers  $A$  and  $B$ : between  $A$  and  $B$  or outside the channel delimited by  $A$  and  $B$ . By assuming the sources  $S$  are distributed over the whole water column. For the case where  $S$  is located between  $A$  and  $B$ , Roux and Fink reached the same conclusion as Eq.2.6 that Green's function estimation is only of a constant factor difference from cross-correlation, but when  $S$  is located outside the channel delimited by  $A$  and  $B$  the difference becomes "the amplitude modulation of each mode by an exponential decrease that depends on the mode number through the attenuation wave number", which leads to an inaccurate contribution of the higher-order modes to the estimated Green's function. Understanding that the feasibility of Lobkis and

Weaver's work depends on the equipartition [59] feature of the interested environment, Roux and Fink specified that the sources  $S$  should span the whole water column and the depth between the neighboring units in sources  $S$  should be such that highest-order mode is correctly sampled because of its significant contribution to Green's function. However, in their numerical simulation, it turns out that even if  $S$  fails to meet those specifications they still obtain a reasonable Green's function estimation. The numerical simulation is performed in both range-dependent and range-independent acoustic channels, and each channel case also has two sources  $S$  configurations as mentioned earlier, so four different configurations were considered. For each configuration,  $A$  is a vertical array of 25 receivers spanning over the water column, and  $B$  is a single receiver at a fixed water depth. While  $S$  keeps as a vertical array of secondary sources spanning over the whole water column, the number of sources is varied (hence also the depth step between each source) to observe its impact to estimation accuracy.

A numerical time-reversal experiment is performed between receivers  $A$  and  $B$  to construct a reference Green's function for accuracy quantification of the estimated Green's function. Roux and Fink pointed out that the correctness of amplitude and phase of the estimated Green's function have different importance as acoustic transmission is concerned: accurate phase with incorrect amplitude is still valuable while the contrary is useless. Beside a classical least-square difference between estimated and reference Green's functions, spatial-temporal representations of the field are presented to address the phase

and amplitude errors respectively by observing the depth and size of focal spot and its side-lobe level. In the case of  $S$  being between  $A$  and  $B$  in the range-independent channel, the focal spot remains focused at the depth of  $B$  and the size does not change as the number of sources  $S$  varies, and even though the side-lobe level does vary with the number of sources it stays low as long as the depth step between sources is no bigger than the smallest wavelength of the source spectrum. This means sufficient number of modes are excited and the depth step needs to be small enough to correctly sample the highest-order mode that has most contribution, as is predicted in their theoretical derivation. And they also showed that significant distortion happens with the focal spot when the sources  $S$  does not span the whole water column, this confirms the orthogonality in Eq.2.2 is essential to make sure modes are equally excited. The standard deviation of the estimation reaches a constant as the number of sources is bigger than a certain number at which the depth step between sources is on the order of the acoustic wavelength. The same result is obtained when sources  $S$  is outside  $A$  and  $B$  as long as  $S$  is not too far away from  $A$  and  $B$  where evanescent waves can make a big impact. Very similar simulation results are found for the range-dependent case.

Roux and Fink showed that Green's function estimation using secondary sources is a robust process as long as the sources have a thorough distribution across the whole water column. Their derivation and simulation are based on the assumption that secondary sources and receivers are coplanar, which is certainly a big limitation considering the real ocean is a three-dimensional environment. Since their work addresses

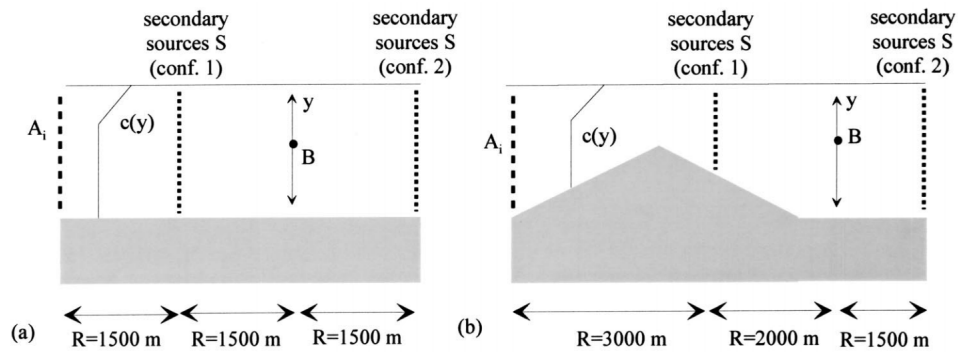


**Figure 2.2:** Acoustic channels used in Roux and Fink's numerical simulation. (a) is for range-independent case where water depth is 100 m and  $B$  is 40 m from the surface; (b) is for range-dependent case where water depth changes from 100 m to 50 m and then back to 100 m from left to right, and  $B$  is at the same water depth as in (a). Adapted from "Greens function estimation using secondary sources in a shallow water environment" by Roux, Philippe and Fink, Mathias. *The Journal of the Acoustical Society of America*, 113(3):1406, 2003.

applications in discrete underwater acoustic communications, secondary sources are of course required. Later Roux et al [35] continued to work on retrieving Green's function without secondary sources, and demonstrated the feasibility of extracting coherent wave fronts from incoherent ambient noises in the ocean. With no identifiable active sources, noises come from every angle and the cross-correlation process follows a directivity pattern: noise sources in the same directivity beam add coherently while those in different directivity beams add incoherently. Their experiment of two sonobuoys in shallow water listening to noises generated by a moving ship shows that only noise sources aligned along the line between the receivers contribute over a long-time correlation. This is because only rays aligned along the receiver axis can pass through both receivers by vertical plane reflection or refraction and thus contribute to constructing the coherent wave fronts between the receivers. In the experiment, when the time window for cross-correlation is short, the

ship track is observable with a low signal-to-noise ratio, and as the time window increases the ship track tends to disappear and a signal of high signal-to-noise ratio is obtained when the ship crosses the end-fire lobes (the beam aligning along the receiver axis). The increasing time window allows more coherent sources contribute to the correlation process, hence leads to a higher signal-to-noise ratio. After the time window reaches some length, the signal-to-noise ratio stops increasing and becomes constant because no more coherent sources are added. With these experiment results, Roux et al simulated and analyzed the ocean environment in three cases: noise sources uniformly distributed throughout the water column; surface noise sources with high frequencies dominant and uniformly distribute over the ocean surface; and low frequency case which is dominated by shipping noise. For the case of shipping noises, the correlation result depends on the specific shipping distribution during the recording time. And for the first two cases, it is shown that the correlation function obtained from ambient noises recored at receivers is a good estimate of the Green's function.

### **2.2.2 Seismology**

The idea of extracting wave propagation information from ambient noise also causes great research interests in seismology. Traditionally, seismologists have used waves that are generated by energetic seismic sources such as earthquake or large explosions to image the earth structure. Large explosions are very expensive and unrealistic and earthquakes are uncertain and usually happen near plate boundaries where observation

stations can be far away from. With these drawbacks, the study of seismic imaging is limited, and seismologists are eager to have an approach to build Green's function from cross-correlating Green's function. Inspired by Lobkis and Weaver, Campillo and Paul first applied the approach by cross-correlating seismic codas [5]. Based on the belief that extracting Green's function from correlation requires the property of modal equipartition of the diffuse field, Campillo and Paul's work relied on the assumption that coda waves, generated by small local earthquakes, are scattered from numerous heterogeneities distributed uniformly in the lithosphere, and the multiple scattering is sufficient to homogenize the space and satisfy the equipartition requirement. With a time-averaged cross-correlation of the coda waves recorded by seismic stations along the west coast of Mexico, Campillo and Paul successfully observed Rayleigh and Love waves. But Snieder [49] argued that Campillo and Paul's work shouldn't be explained by equipartition of modes: modes are either the normal modes of Earth or the surface wave modes that propagate along the Earth's surface, in Campillo and Paul's study, if the Earth's modes are invoked then the time is too short for the Earth's normal modes to equilibrate; if the surface wave modes are invoked, they exist for every frequency and due to the shallow depth of most earthquakes most of the energy is carried by the fundamental Love and Rayleigh modes, so equipartition of modes can't be established. However, Snieder did not deny the feasibility of extracting Green's function with coda waves proved by Campillo and Paul instead he presented an alternative derivation to show that global equipartition of normal modes is not always necessary and can be reduced to a requirement that the scattered waves

propagated on average isotropically near the receivers, which is very similar to the finding by Roux et al [35] that noise sources along the line between the receivers contribute to a long-time correlation. Having the receivers in a medium of scatters  $s$  radiating scalar waves, Snieder expressed the cross-correlation as a double sum  $\sum_{s,s'}$  over all scatters, which can be split into a sum over diagonal terms  $\sum_{s=s'}$  and a sum over cross terms  $\sum_{s \neq s'}$ . When averaged over time and different sources, the cross term can be ignored by increasing the time interval and the number of sources, hence the main contribution to cross-correlation comes from the region of constructive interference along the source-receiver line. Because Snieder's derivation does not rely on normal modes, it is equally valid for both closed and open systems as long as the local condition on the isotropic propagation of waves along the receiver line is satisfied.

While the approach with coda waves works, it still depends on the occurrence of earthquakes. Shapiro and Campillo [44] suggested to retrieve Green's function from correlations of the ambient seismic noise instead of coda waves. The advantage of ambient seismic noise over coda waves is twofold: ambient seismic noise is mainly excited by shallow sources such as ocean microseisms and atmospheric perturbations thus requires no earthquake at all; large and dense networks of broadband seismic sensors are commonly used for earthquake monitoring worldwide and the recording for ambient seismic noise is continuous for any direction of propagation. The distribution of the ambient sources become random over a long-time period average and the seismic noise can be considered as a random field such that the equipartition property of normal modes is established.

Shapiro and Campillo obtained very satisfying results by correlating the ambient seismic noise recorded during a period when no large earthquake happened and compared with the predictions through global velocity maps constructed by body waves. They also achieved great results in constructing tomographic images of the major geologic units in California with the same technique [45]. And a similar study conducted by Sabra et al [41] in Southern California further validates the approach of Green's function estimation from ambient noise. A recent paper entitled "Imaging with ambient noise" by Snieder and Wapenaar [51] presents comprehensive summary about Green's function retrieval from ambient noise. It discusses the development of the approach in various areas during the past decade, outlines the governing principle derived by Lobkis and Weaver, and assures the feasibility of the approach in both closed and open systems. By studying various research and industrial production examples in many different fields, Snieder and Wapenaar showed that the approach is not constrained to one particular area but widely applicable to environments that are governed by linear equations, and thus many more applications are yet to be discovered.

# Chapter 3

## Theoretical Derivations

In this chapter, we provide mathematical proof for Eq.1.4 for two kinds of environments, i.e. open and closed systems. The material in this chapter was taken from Brown and Lu [3]. Section 3.1 introduces relevant GF definitions and lays the groundwork for the later derivations. Section 3.2 presents a general derivation that works for both open and closed systems, and section 3.3 presents an alternative derivation specially for closed systems.

### 3.1 Preliminaries

There are many different GFs throughout this chapter, and it is important to distinguish between them.  $G_\phi$  is the velocity potential GF evaluated at free surface, and  $G_\eta$  is the surface elevation GF. Both of them have time and frequency domain representations. There are two important operations in Eq.1.4, cross-correlation on the left-hand side and convolution on the right-hand side. And they are in fact closely related to each other. Let

$f_1(t)$  and  $f_2(t)$  denote two real-valued functions in time domain, then convolution of  $f_1(t)$  and  $f_2(t)$  is defined as

$$f_1(t) * f_2(t) = \int_{-\infty}^{\infty} d\tau f_1(\tau) f_2(t - \tau), \quad (3.1)$$

and the cross-correlation of  $f_1(t)$  and  $f_2(t)$  is defined as

$$C(t) = \int_{-\infty}^{\infty} d\tau f_1(\tau) f_2(t + \tau) = f_1(t) * f_2(-t). \quad (3.2)$$

Now let  $\bar{f}(\omega)$  denote the frequency domain representation of  $f(t)$ , which is obtained by performing Fourier transform on  $f(t)$

$$\bar{f}(\omega) = F[f(t)] = \int_{-\infty}^{\infty} f(t) e^{i\omega t} dt, \quad (3.3)$$

then  $f(t) = F^{-1}[\bar{f}(\omega)]$  (inverse Fourier transform). Because variables are all real-valued,  $\bar{f}(-\omega)$  is equal to its complex conjugate  $\bar{f}^*(\omega)$ . So we have the following equalities:

$$\left\{ \begin{array}{l} F[f_1(t) * f_2(t)] = \bar{f}_1(\omega) \bar{f}_2(\omega) \\ F[f_1(t) * f_2(-t)] = \bar{f}_1(\omega) \bar{f}_2^*(\omega) \end{array} \right. \quad (3.4)$$

Note that in practice cross-correlation is done over two finite time series, therefore we change the integration bound in Eq.3.2 to  $T$  and come to

$$f_1(t) \star f_2(-t) = \int_0^T d\tau f_1(\tau) f_2(t + \tau), \quad (3.5)$$

where  $\star$  denotes correlation with finite bounds.

The starting point of the derivations is to solve the linearized water wave equations of motion with boundary conditions at free surface and bottom. Suppose  $\mathbf{x} = (x, y)$  is the lateral vector and vertical coordinate  $z = 0$  at free surface. For an irrotational flow,  $\mathbf{u}(\mathbf{x}, z, t) = \nabla\Phi(\mathbf{x}, z, t)$ . With this assumption the continuity equation for an incompressible flow with source  $f(\mathbf{x}, z, t)$  is  $\nabla^2\Phi(\mathbf{x}, z, t) = f(\mathbf{x}, z, t)$ . The kinematic bottom condition is  $\partial\Phi/\partial z = 0$  at  $z = -h$ , the kinematic free surface condition is  $\partial\eta/\partial t = \partial\Phi/\partial z$  at  $z = 0$ , and the dynamic free surface condition is  $g\eta + \partial\Phi/\partial t = 0$  at  $z = 0$ . So the problem is to solve

$$\begin{aligned} \nabla^2\Phi(\mathbf{x}, z, t) &= f(\mathbf{x}, z, t) \\ \frac{\partial^2\Phi}{\partial^2t} + g\frac{\partial\Phi}{\partial z} &= 0, \quad z = 0 \\ \frac{\partial\Phi}{\partial z} &= 0, \quad z = -h \end{aligned} \quad (3.6)$$

where

$\nabla^2$  : three dimensional Laplacian operator,

$\nabla_{\perp}$  : two dimensional gradient operator,

$\nabla_{\perp}^2$  : two dimensional Laplacian operator,

$h$  : water depth, constant,

$\Phi(\mathbf{x}, z, t)$  : velocity potential,

$\bar{\Phi}(\mathbf{x}, z, \omega)$  : Fourier transform of the velocity potential,

$f(\mathbf{x}, z, t)$  : source function.

We assume here that the depth dependence of source function  $f(x, z, t)$  is chosen to couple naturally to surface gravity waves with small amplitudes so it allows the free surface and bottom boundary conditions to be satisfied. Transformed to the frequency domain, Eq.3.6 becomes

$$\begin{aligned}\nabla^2 \bar{\Phi}(\mathbf{x}, z, \omega) &= \bar{f}(\mathbf{x}, z, \omega) \\ \omega^2 \bar{\phi} &= g \frac{\partial \bar{\Phi}}{\partial z}, \quad z = 0 \\ \frac{\partial \bar{\Phi}}{\partial z} &= 0, \quad z = -h\end{aligned}\tag{3.7}$$

Given the dispersion relation  $\omega^2 = gk \tanh kh$ , the problem can be reduced to solving

$$(\nabla_{\perp}^2 + k^2) \bar{\phi}(\mathbf{x}, \omega) = \bar{p}(\mathbf{x}, \omega)\tag{3.8}$$

by assuming that  $\bar{f}(\mathbf{x}, z, \omega) = \bar{p}(\mathbf{x}, \omega) \cosh k(z+h) / \cosh kh$  and  $\bar{\Phi}(\mathbf{x}, \omega) = \bar{\phi}(\mathbf{x}, \omega) \cosh k(z+h) / \cosh kh$ . And the solution is  $\phi(\mathbf{x}, \omega) = \iint d\mathbf{x}' \bar{G}_{\phi}(\mathbf{x}|\mathbf{x}', \omega) \bar{p}(\mathbf{x}', \omega)$  where  $G_{\phi}(\mathbf{x}|\mathbf{x}', \omega)$  is the GF for two dimensional Helmholtz equation

$$(\nabla_{\perp}^2 + k^2) \bar{G}_{\phi}(\mathbf{x}|\mathbf{x}', \omega) = \delta(\mathbf{x} - \mathbf{x}')\tag{3.9}$$

Here we also give the definition of surface elevation GF  $\bar{G}_\eta(\mathbf{x}|\mathbf{x}', \omega)$ ,

$$\bar{\eta}(\mathbf{x}, \omega) = \iint d\mathbf{x}' \bar{G}_\eta(\mathbf{x}|\mathbf{x}', \omega) \bar{p}(\mathbf{x}', \omega) \quad (3.10)$$

which is defined by the relationships  $\bar{\eta}(\mathbf{x}, \omega) = (i\omega/g)\bar{\phi}(\mathbf{x}, \omega)$  and  $\bar{G}_\eta(\mathbf{x}|\mathbf{x}', \omega) = (i\omega/g)\bar{G}_\phi(\mathbf{x}|\mathbf{x}', \omega)$ . In the time domain the corresponding form is

$$\eta(\mathbf{x}, t) = \iint d\mathbf{x}' G_\eta(\mathbf{x}|\mathbf{x}', t) * p(\mathbf{x}', t) \quad (3.11)$$

where  $G_\eta(\mathbf{x}|\mathbf{x}', t) = (-1/g)(\partial/\partial t)G_\phi(\mathbf{x}|\mathbf{x}', t)$ .

## 3.2 General derivation

Now we proceed to derive GF identity that leads to Eq.1.4. When weak dissipation is allowed in the system, Eq.3.8 becomes  $(\nabla_\perp^2 + k^2 + i\omega\epsilon)\bar{G}_\phi(\mathbf{x}|\mathbf{x}', \omega) = \delta(\mathbf{x} - \mathbf{x}')$  assuming the dissipation is proportional to  $\omega\epsilon$ . Then  $\bar{G}_\phi$  at point  $\mathbf{x}$  due to impulsive source excitation at  $\mathbf{x}_A$  satisfies

$$(\nabla_\perp^2 + k^2 + i\omega\epsilon)\bar{G}_\phi(\mathbf{x}|\mathbf{x}_A, \omega) = \delta(\mathbf{x} - \mathbf{x}_A). \quad (3.12)$$

and  $\bar{G}_\phi$  at point  $\mathbf{x}$  due to impulsive source excitation at  $\mathbf{x}_B$  satisfies

$$(\nabla_\perp^2 + k^2 + i\omega\epsilon)\bar{g}_\phi(\mathbf{x}|\mathbf{x}_B, \omega) = \delta(\mathbf{x} - \mathbf{x}_B). \quad (3.13)$$

because of reciprocity,  $\bar{\phi}(\mathbf{x}|\mathbf{x}_A, \omega) = \bar{\phi}(\mathbf{x}_A|\mathbf{x}, \omega)$  and  $\bar{\phi}(\mathbf{x}|\mathbf{x}_B, \omega) = \bar{\phi}(\mathbf{x}_B|\mathbf{x}, \omega)$ . We multiply Eq.3.12 by  $\bar{g}_\phi^*(\mathbf{x}_B|\mathbf{x}, \omega)$ , integrate over  $\mathbf{x}$ , and take complex-conjugate on both sides to arrive to

$$\iint d\mathbf{x} \bar{G}_\phi(\mathbf{x}_B|\mathbf{x}, \omega) (\nabla_\perp^2 + k^2 - i\omega\epsilon) \bar{G}_\phi^*(\mathbf{x}_A|\mathbf{x}, \omega) = \bar{G}_\phi(\mathbf{x}_B|\mathbf{x}_A, \omega). \quad (3.14)$$

And We multiply Eq.3.13 by  $\bar{G}_\phi^*(\mathbf{x}_A|\mathbf{x}, \omega)$ , integrate over  $\mathbf{x}$ , and take complex-conjugate on both sides to arrive to

$$\iint d\mathbf{x} \bar{G}_\phi(\mathbf{x}_A|\mathbf{x}, \omega) (\nabla_\perp^2 + k^2 + i\omega\epsilon) \bar{G}_\phi^*(\mathbf{x}_B|\mathbf{x}, \omega) = \bar{G}_\phi(\mathbf{x}_A|\mathbf{x}_B, \omega). \quad (3.15)$$

Subtracting Eq.3.15 Eq.3.14 yields

$$Q - 2i\omega\epsilon \iint d\mathbf{x} \bar{G}_\phi(\mathbf{x}_B|\mathbf{x}, \omega) \bar{G}_\phi^*(\mathbf{x}_A|\mathbf{x}, \omega) = \bar{G}_\phi(\mathbf{x}_B|\mathbf{x}_A, \omega) - \bar{G}_\phi^*(\mathbf{x}_A|\mathbf{x}_B, \omega), \quad (3.16)$$

where

$$Q = \iint d\mathbf{x} \bar{G}_\phi(\mathbf{x}_B|\mathbf{x}, \omega) \nabla_\perp^2 \bar{G}_\phi^*(\mathbf{x}_A|\mathbf{x}, \omega) - \iint d\mathbf{x} \bar{G}_\phi^*(\mathbf{x}_A|\mathbf{x}, \omega) \nabla_\perp^2 \bar{G}_\phi(\mathbf{x}_B|\mathbf{x}, \omega) \quad (3.17)$$

Applying the divergence theorem onto Eq.3.17, we get the second form of  $Q$ :

$$Q = \oint dl [\bar{G}_\phi(\mathbf{x}_B|\mathbf{x}, \omega) \nabla_\perp \bar{G}_\phi^*(\mathbf{x}_A|\mathbf{x}, \omega) - \bar{G}_\phi^*(\mathbf{x}_A|\mathbf{x}, \omega) \nabla_\perp \bar{G}_\phi(\mathbf{x}_B|\mathbf{x}, \omega)] \cdot \hat{n} \quad (3.18)$$

where  $\oint$  denotes a line integral over the domain boundary and  $\hat{n}$  is its unit normal vector. Now consider appropriate conditions of  $\mathbf{x}$  for both open and closed systems. For open ocean, we can set the domain as a circle of large radius  $R$  with the midpoint of  $\mathbf{x}_A$  and  $\mathbf{x}_B$  as its center. In this scenario,  $Q$  approaches to 0 when  $R$  is large because  $\bar{G}_\phi$  and  $\nabla_\perp \bar{G}_\phi \cdot \hat{n}$  approach to 0 faster than  $R^{-1/2}$ . For closed system, we set the domain as a rectangular wave tank,  $Q$  is equal to 0 because  $\nabla_\perp \bar{G}_\phi = 0$  at the rigid walls. So for both open and closed systems  $Q = 0$ . Now Eq.3.16 becomes

$$-2i\omega\epsilon \iint d\mathbf{x} \bar{G}_\phi(\mathbf{x}_B|\mathbf{x}, \omega) \bar{G}_\phi^*(\mathbf{x}_A|\mathbf{x}, \omega) = \bar{G}_\phi(\mathbf{x}_B|\mathbf{x}_A, \omega) - \bar{G}_\phi^*(\mathbf{x}_A|\mathbf{x}_B, \omega), \quad (3.19)$$

which in time domain corresponds to

$$2\epsilon \frac{d}{dt} \iint d\mathbf{x} G_\phi(\mathbf{x}_B|\mathbf{x}, t) * G_\phi(\mathbf{x}_A|\mathbf{x}, -t) = G_\phi(\mathbf{x}_B|\mathbf{x}_A, t) - G_\phi(\mathbf{x}_B|\mathbf{x}_A, -t), \quad (3.20)$$

Recall that  $\bar{\eta}(\mathbf{x}, \omega) = (i\omega/g)\bar{\phi}(\mathbf{x}, \omega)$ ,  $\bar{G}_\eta = (i\omega/g)\bar{G}_\phi$  and  $G_\eta = (-1/g)\partial G_\phi/\partial t$ , applying these relationships to Eq.3.19 and Eq.3.20 we get the equivalent equations for surface elevation:

$$2\epsilon g \iint d\mathbf{x} \bar{G}_\eta(\mathbf{x}_B|\mathbf{x}, \omega) \bar{G}_\eta^*(\mathbf{x}_A|\mathbf{x}, \omega) = \bar{G}_\eta(\mathbf{x}_B|\mathbf{x}_A, \omega) + \bar{G}_\eta^*(\mathbf{x}_A|\mathbf{x}_B, \omega), \quad (3.21)$$

and

$$2\epsilon g \iint d\mathbf{x} G_\eta(\mathbf{x}_B|\mathbf{x}, t) * G_\eta(\mathbf{x}_A|\mathbf{x}, -t) = G_\eta(\mathbf{x}_B|\mathbf{x}_A, t) + G_\eta(\mathbf{x}_B|\mathbf{x}_A, -t), \quad (3.22)$$

Eq.3.22 is the GF identity that underlies Eq.1.4. Note that on the left hand side of Eq.3.22 the dissipation parameter  $\epsilon$  should be nonzero to avoid the scenario of zero times the non-divergent integration over unbounded domain. However, for the purpose of testing via numerical and experimental methods (in later chapters), one can safely ignore dissipation because both spatial and time domains will be finite and we only need to prove the proportionality of the left- and right-hand sides.

In an unbounded domain and when  $\epsilon$  approaches 0, we have

$$\bar{G}_\phi(\mathbf{x}|\mathbf{x}_0, \omega) = (-i/4)H_0^{(1)}(k(\omega)r), \quad (3.23)$$

where  $r = |\mathbf{x} - \mathbf{x}_0|$  and  $H_0^1$  is the Hankel function of the first kind. So in time domain

$$\bar{G}_\phi(\mathbf{x}|\mathbf{x}_0, t) = F^{-1}\left[-\frac{i}{4c_g(k(\omega))}H_0^1(k(\omega)r)\right], \quad (3.24)$$

which is only analytically solvable for nondispersive  $k(\omega)$ . Note this does not affect the validity of Eq.3.21 and Eq.3.22 where dispersive  $k(\omega)$  applies.

Now we focus on the cross-correlation on the left-hand side of Eq.1.4, which is an approximate result that relies on statistical assumptions. Substituting  $\mathbf{x}_A$  and  $\mathbf{x}_B$  into Eq.3.11, we can write the surface elevations at both locations as:

$$\begin{aligned} \eta(\mathbf{x}_A, t) &= \iint d\mathbf{x} G_\eta(\mathbf{x}_A|\mathbf{x}, t) * p(\mathbf{x}, t), \\ \eta(\mathbf{x}_B, t) &= \iint d\mathbf{x} G_\eta(\mathbf{x}_B|\mathbf{x}, t) * p(\mathbf{x}, t). \end{aligned} \quad (3.25)$$

Following the definition of cross-correlation, we have

$$C_{\mathbf{AB}} = \iiint d\mathbf{x} \iiint d\mathbf{x}' G_{\eta}(\mathbf{x}_A|\mathbf{x}, t) * G_{\eta}(\mathbf{x}_B|\mathbf{x}', -t) * p(\mathbf{x}, t) * p(\mathbf{x}', -t). \quad (3.26)$$

We now assume source function  $p(\mathbf{x}, t)$  is delta-related in space and almost delta-related in time,

$$p(\mathbf{x}, t) * p(\mathbf{x}', -t) = a^2 \delta(\mathbf{x} - \mathbf{x}') D(t), \quad (3.27)$$

where  $a$  is a constant with dimension m and  $D(t)$  is a band-limited function that approximates to delta function. And following relationships are satisfied:

$$D(t) = d(t) * d(-t), \quad (3.28)$$

$$\bar{D}(\omega) = \bar{d}(\omega) d^*(\omega) = |\bar{d}(\omega)|^2,$$

where  $d(t)$  is the time record of a single source excitation and  $\bar{d}(\omega)$  is its frequency domain correspondence. It is clear that  $D(t)$  has zero phase and approaches  $\delta(t)$  when bandwidth is unlimited.

With Eq.3.27, Eq.3.26 reduces to

$$C_{\mathbf{AB}} = a^2 D(t) \iiint d\mathbf{x} G_{\eta}(\mathbf{x}_A|\mathbf{x}, t) * G_{\eta}(\mathbf{x}_B|\mathbf{x}', -t), \quad (3.29)$$

which together with Eq.3.22 leads to

$$\frac{2\epsilon g}{a^2} C_{\mathbf{AB}} = D(t) * [G_{\eta}(\mathbf{x}_B|\mathbf{x}_A, t) + G_{\eta}(\mathbf{x}_B|\mathbf{x}_A, -t)]. \quad (3.30)$$

It is worth noting that while Eq.3.30 is equivalent to Eq.3.22 with a detailed  $\gamma$ , Eq.3.22 is valid without requiring the statistical assumption (Eq.3.27) which is essential for the validity of Eq.3.30. Also, in our numerical results, the cross-correlation is evaluated as  $\eta(\mathbf{x}_A, t) \star \eta(\mathbf{x}_B, t)$  over finite time domains.

### 3.3 Closed system derivation

Now we present another derivation regarding the closed system, more specifically a wave tank geometry. While in the previous section we covered both open and closed systems with more general derivations, it is necessary to solve the problem using a different approach. Reaching to the same conclusion from different perspectives is a great way to confirm the validity of the conclusion itself. Furthermore this alternative derivation will provide important references as we conduct simulations and experiments based on wave tank geometry.

We set the geometry as a rectangular wave tank with width  $L_x$ , length  $L_y$  and water depth  $h$ , and also let vertical coordinate  $z = 0$  at free surface. The problem is to solve linearized wave equation with boundary conditions:

$$\begin{aligned} \nabla^2 \Phi &= 0, \\ \Phi_x &= 0, \quad x = 0, x = L_x; \quad \Phi_y = 0, \quad y = 0, y = L_y \\ \Phi_z &= 0, \quad z = -h; \quad \Phi_z = (\omega^2/g)\Phi, \quad z = 0 \end{aligned} \tag{3.31}$$

Using modes the velocity potential can be expressed as

$$\Phi(\mathbf{x}, t) = \sum_{l,m} \frac{\cosh k_{lm}(z+h)}{\cosh k_{lm}h} \cos \frac{l\pi x}{L_x} \cos \frac{m\pi y}{L_y} (a_{lm} \cos \omega_{lm}t + b_{lm} \sin \omega_{lm}t), \quad (3.32)$$

where  $l$  and  $m$  are the mode numbers along the tank and across the tank. Mode numbers and wave number satisfy the relationship  $k_{lm}^2 = (l\pi/L_x)^2 + (m\pi/L_y)^2$  and the dispersion relation in modes is  $\omega_{lm}^2 = gk_{lm} \tanh k_{lm}h$ . With free surface boundary condition  $\Phi_z = \partial\eta/\partial t$  at  $z = 0$ , we can compute  $\eta(x, y, t)$ :

$$\eta(x, y, t) = \sum_l \sum_m \omega_{lm} \cos \frac{l\pi x}{L_x} \cos \frac{m\pi y}{L_y} (a_{lm} \sin \omega_{lm}t - b_{lm} \cos \omega_{lm}t) \quad (3.33)$$

Assume the source function in Eq.3.11 has form of  $p(\mathbf{x}, t) = A_0\delta(\mathbf{x} - \mathbf{x}_0)\delta(t)$ , then  $G_\eta(\mathbf{x}|\mathbf{x}_0, t)$  is  $1/A_0$  times a particular  $\eta(\mathbf{x}, t)$ , where  $A_0$  has dimension m. The physical meaning of the source function is instantaneous water injection of volume  $V_0 = L_0A_0$  at  $\mathbf{x} = \mathbf{x}_0, t = 0$ . So we have to construct the initial value conditions to solve for  $G_\eta(\mathbf{x}|\mathbf{x}_0, t)$ :

$$\begin{aligned} \eta(\mathbf{x}, 0) &= V_0\delta(\mathbf{x} - \mathbf{x}_0), \\ \frac{\partial\eta(\mathbf{x}, t)}{\partial t}(x, 0) &= 0. \end{aligned} \quad (3.34)$$

Solving the above problem, we obtain the surface elevation GF in modal form as

$$G_\eta(\mathbf{x}|\mathbf{x}', t) = \frac{L_0}{L_x L_y} H(t) \sum_l \sum_m m\beta_l\beta_m \cos \frac{l\pi x}{L_x} \cos \frac{m\pi y}{L_y} \cos \frac{l\pi x'}{L_x} \cos \frac{m\pi y'}{L_y} \cos \omega_{lm}t, \quad (3.35)$$

where  $\beta_l = 1$  for  $l = 0, 2$  otherwise, and  $H(t)$  is the Heaviside step function. And constants  $a_{lm}$  and  $b_{lm}$  in Eq.3.33 are solved using the orthogonality of the modes. Eq.3.35 can be generalized to

$$G_\eta(\mathbf{x}|\mathbf{x}', t) = \frac{L_0}{A} H(t) \sum_n \psi_n(\mathbf{x}) \psi_n(\mathbf{x}') \cos \omega_n t. \quad (3.36)$$

Here  $A$  is the lateral area of the domain, and eigenfunction of orthogonal modes  $\psi_n(\mathbf{x})$  satisfies  $\iint d\mathbf{x} \psi_n(\mathbf{x}) \psi_m(\mathbf{x}) = A \delta_{nm}$ . After some algebra Eq.3.36 results in

$$\iint d\mathbf{x} G_\eta(\mathbf{x}_A|\mathbf{x}, t) \star G_\eta(\mathbf{x}_B|\mathbf{x}, t) = \frac{L_0}{A} \sum_n \psi_n(\mathbf{x}_A) \psi_n(\mathbf{x}_B) [H(t) \cos \omega_n t \star H(t) \cos \omega_n t]. \quad (3.37)$$

where  $H(t) \cos \omega_n t \star H(t) \cos \omega_n t$  reduces to, over a finite time period  $T$ ,

$$H(t) \cos \omega_n t \star H(t) \cos \omega_n t = T \cos \omega_n t \left( 1 + \frac{\sin \omega_n T \cos \omega_n T}{\omega_n T} \right). \quad (3.38)$$

We assume  $\omega_n T$  is large so the part in parenthesis in Eq.3.38 is approximated to 1.

Combining Eq.3.37 and Eq.3.36 gives

$$\frac{L_0}{T} \iint d\mathbf{x} G_\eta(\mathbf{x}_A|\mathbf{x}, t) \star G_\eta(\mathbf{x}_B|\mathbf{x}, t) = G_\eta(\mathbf{x}_A|\mathbf{x}_B, t) + G_\eta(\mathbf{x}_A|\mathbf{x}_B, -t). \quad (3.39)$$

As one can tell, Eq.3.39 is almost the same as Eq.3.22 except the difference of an constant, which is nonessential because the proportionality is enough as we mentioned earlier.

Now we focus on cross-correlation of surface elevations in the wave tank geometry.

Generally a random wave field described as a superposition of modes follows

$$\eta(\mathbf{x}, t) = d(t) * \sum_n (c_n \cos \omega_n t + d_n \sin \omega_n t) \psi_n(\mathbf{x}). \quad (3.40)$$

where  $d(t)$  modulates the wave field to a limited bandwidth. Note we assume phases are random which means

$$\langle c_n c_m \rangle = \langle d_n d_m \rangle = a^2 \delta_{nm}, \langle c_n d_m \rangle = 0 \quad (3.41)$$

where  $\langle \rangle$  is the ensemble average. Despite that  $d(t)$  carries phase information, it is not manifested in  $\eta(\mathbf{x}, t)$  because of the random phases, which is consistent with the argument in the previous section that  $D(t)$  has contains no phase information from  $d(t)$ . Naturally we define cross-correlation as

$$C_{AB}(t) = \left\langle \int_0^T d\tau \eta(\mathbf{x}_A, \tau) \eta(\mathbf{x}_B, \tau + t) \right\rangle. \quad (3.42)$$

Combining Eq.3.40 and Eq.3.42, and applying the statistical properties denoted in Eq.3.41 gives

$$C_{AB}(t) = D(t) * a^2 T \sum_n \psi_n(\mathbf{x}_A) \psi_n(\mathbf{x}_B) \cos \omega_n t, \quad (3.43)$$

where  $D(t) = d(t) * d(-t)$ . Substituting Eq.3.36 into the equation above yields

$$\frac{L_0}{Aa^2T}C_{AB}(t) = D(t) * [G_\eta(\mathbf{x}_B|\mathbf{x}_A, t) + G_\eta(\mathbf{x}_B|\mathbf{x}_A, -t)] \quad (3.44)$$

We reach to the same proportional result as in the previous section, which concludes our alternative derivation for a closed system.

# Chapter 4

## Numerical Simulations

In the previous chapter, theoretical derivations are provided respectively in both open and closed systems, so in this chapter it is sensible (from the perspective of completeness) to simulate both environments through numerical methods to support each of the derivations. It may seem natural to focus solely on the open system since it is arguably a better representation of the most commonly interested water wave fields in the open ocean. However, as reviewed in Chapter 2, many previous research works on GF retrieval via cross-correlation investigated closed systems with success, it is obligatory to devote the same effort in the context of a water wave field. More importantly, including the case of a closed system provides important alternative validation for the research topic and also provides additional demonstration for the generality of the modal derivation.

Although the details of two following simulations differ in many aspects such as geometry and surface elevation generation, on a high level both simulations follow very similar procedures:

- simulate the random surface gravity water wave field
- choose two locations in the field and record the surface elevations for a certain period of time
- correlating the signals ("noise") recorded at the receivers
- compute the GF between the receivers and compare with the correlation result

For the case of an open system, the property of "open" is hard to implement numerically, instead a unbounded circular environment with two receivers placed along a diameter and being symmetric with the center make a good approximation as long as the diameter is significantly larger than the distance between the receivers. Point sources are randomly distributed inside the large circle and at each source location an impulse is excited at a time stamp that is also randomly distributed during the recording time period. Since surface gravity waves are mostly interested, it is proper to assume that the ratio of wave height to wavelength is small. Deep water condition is also assumed and the closed system simulation has the same assumption. The receivers around the center record simulated surface waves coming from all directions with various wavelengths, therefore the recorded signal exhibits no particular pattern but randomness as of noise. Previous studies reviewed in Chapter 2 show that a good GF estimation requires a long-time averaged cross-correlation, but quantitative specification of how long the recording time should be is not found, as a matter of fact, the exact time length could vary much depending on different problems and domain parameters. For the simulation in this thesis work different recording time lengths are tried and one such that longer recording does not improve the correlation

result much is chosen. The simulated GF is the recorded response at one receiver when an impulse is excited only at the other receiver.

For a closed system simulation, a rectangular wave tank geometry is simulated to be consistent with the theoretical derivation. Since later in Chapter 6 an experiment is in the wave tank presented, the tank parameters in the simulation is set accordingly to the actual experiment. In Chapter 2 it is shown that a global equipartition condition of the studied environment leads to successful GF retrieval. Equipartition means all normal modes have uncorrelated amplitudes with equal mean squares, this is not hard to achieve once surface elevations are expressed in modes. However, surface gravity waves in reality does not have an equipartition property, and because most of its energy is in a low frequency band, a weight function is applied on the modes so that surface gravity waves are simulated properly. Fortunately, as Roux et al [35] and Snieder [49] pointed out, equipartition is not necessary and the main contribution is from the waves that propagate along the receiver axis. As to GF, since its explicit expression is solved for such geometry in the derivation, it is easy to generate once the modes are simulated.

## 4.1 Open system simulation

In this simulation a two dimensional square grid which is 1000 m in both length and width is created to represent a laterally unbounded domain. A set of 100000 point sources are randomly distributed in a circle of radius  $R = 500$  m on the grid and two receivers  $A$  and  $B$  are located around the center of the grid with a separation of 100 m. With the center of the

circle as the origin, the coordinates of the two receivers are accordingly  $A(-50\text{ m}, 0\text{ m})$ ,  $B(50\text{ m}, 0\text{ m})$ , as shown in Fig.4.1. The coordinates of the receivers are so chosen that the distance in between (100 m) is rather small compared to the circle diameter (1000 m). Under this configuration, the longest possible distance  $r$  between a receiver and a source (the farthest one to its left/right) is 550 m. This number is important because it implies the maximum time delay of the waves that generated at the all sources traveling to the receivers, and therefore decides the cross-correlation time window length. Fig.4.1 shows the geometry and source distribution.

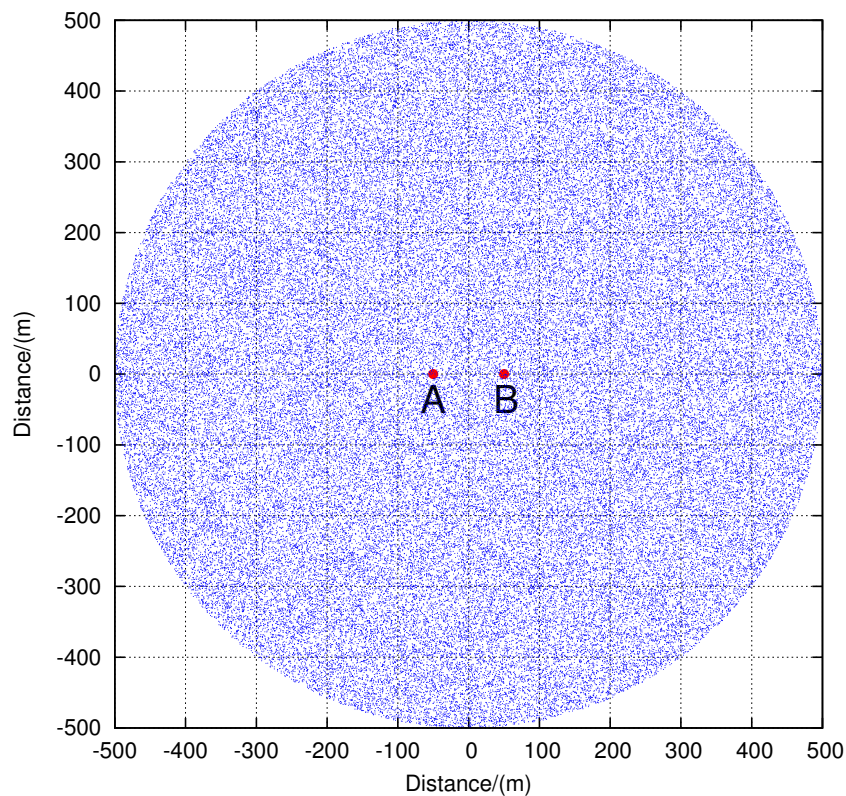


**Figure 4.1:** 100000 sources (blue dots) are randomly distributed in a circular region whose radius is 500 m. Two receivers  $A$  and  $B$  (red dots) are centered around the origin and 100 m away from each other.

When an impulsive point source is excited, with the linear theory approximation each spectral component propagates independent of the others. Recall that  $\bar{G}_\eta = (i\omega/g)\bar{G}_\phi$ , and that in an unbounded domain,

$$\bar{G}_\phi(\mathbf{x}|\mathbf{x}_0, \omega) = -\frac{i}{4}H_0^{(1)}(k(\omega)r) \quad (4.1)$$

where  $r = |\mathbf{x} - \mathbf{x}_0|$ ,  $k = (k_x^2 + k_y^2)^{1/2}$  is the amplitude of the wavenumber vector, and  $H_0^{(1)}(kr)$  is the Hankel function of the first kind, whose large argument asymptotic expression is

$$H_0^{(1)}(kr) \simeq \sqrt{\frac{2}{\pi kr}} e^{i(kr - \pi/4)} \quad (4.2)$$

we also assume that water depth  $h$  is sufficiently large ( $kh \gg 1$ ) that the deep water dispersion relation,

$$\omega^2 = gk \quad (4.3)$$

holds over the excited frequency band, here  $g$  is the gravitational acceleration. With Eq.4.1, Eq.4.2 and Eq.4.3 combined, it follows that

$$G_\eta(\mathbf{x}|\mathbf{x}_0, t) = \frac{1}{4gh} F^{-1} \left[ \frac{\omega}{c_g(k(\omega))} H_0^{(1)}(\omega^2 r/g) \right] \quad (4.4)$$

where  $F^{-1}$  is the inverse Fourier transform.

To better resemble surface gravity waves in the open ocean, it is reasonable to confine energy of the point source response to a limited band, so the response is computed as  $d(t) *$

$G_\eta(\mathbf{x}|\mathbf{x}_0, t)$ , where  $d(t)$  is the weighting function that modulates the energy distribution of the different spectral components. For numerical purpose,  $\bar{d}(\omega)$ , which is the counterpart in frequency domain of  $d(t)$ , is set as

$$\bar{d}(\omega) = \omega^2 e^{-(\omega/\omega_0)^2} \quad (4.5)$$

with the peak angular frequency  $\omega_0 = 2\pi \times 0.1$  Hz, and the wave frequencies,  $f = \omega/2\pi$ , are limited to the bandwidth  $0 < f < 0.5$  Hz. The convolution  $d(t) * G_\eta(\mathbf{x}|\mathbf{x}_0, t)$  corresponds to  $\bar{d}(\omega)\bar{G}_\phi(\mathbf{x}|\mathbf{x}_0, \omega)$  in frequency domain. Therefore for each individual point source excitation the response is simulated as  $F^{-1}[\bar{b}(\omega)]$ ,

$$\bar{b}(\omega) = \frac{\bar{d}(\omega)\omega}{c_g(k(\omega))} H_0^{(1)}(\omega_2 r/g) \quad (4.6)$$

To insure that after inverse Fourier transform  $d(t) * G_\eta(\mathbf{x}|\mathbf{x}_0, t)$  is real, the condition  $\bar{b}(-\omega) = \bar{b}^*(\omega)$  is applied in the numerical simulation.

Because of dispersion in water wave field, an impulse signal will "unwrap" into waves of different frequencies. And these waves have different speed and arrive at the same location at different times. With the deep water dispersion relation Eq.4.3, the relationship between phase velocity  $c_p$  and angular frequency  $\omega$  can be determined:

$$c_p = \frac{g}{\omega} \quad (4.7)$$

It follows that the long waves with low frequencies travel faster than the short waves with high frequencies, therefore arrives at the receiver earlier. Since a band-limited function is applied and the maximum frequency is 0.5 Hz, the wave with minimum phase speed is computed to travel at 3.12 m/s based on Eq. 4.7. The wave envelope travels at the group speed which is half the phase speed in deep water. Dividing the maximum distance (550 m) between the receiver and any point source by the minimum wave group speed, we get a threshold for the time window, which is about 353 s. In principle a time window longer than 353 s will include all the waves of different frequencies. Now we decide how the inverse Fourier transform is performed. Nyquist sampling theorem states that the sampling frequency should be at least two times the highest frequency (0.5 Hz), so in our case the sampling frequency should at least be 1 Hz. For better practice, we set the sampling frequency to be 2 Hz, therefore the time series of response has a resolution of 0.5 s and a total of 706 sampling points. For the purpose of FFT, we adjust the number of sampling points in frequency domain to 2048, which leads the time window to be 512 s. This time window means that for each individual impulse source the receiver records the waves for a total time length of 512 s once the source is excited. The actual surface elevation at the receivers is a superposition of all the waves generated by all the points sources. In order to simulate the randomness of the wave field, we also distribute the excitation time of each point sources in a time span of 10240 s. The superposed time sequence is the simulated surface elevation at the receiver, and will be used for cross-correlation. Fig 4.2 shows the

simulated surface elevations at both receiver locations. They are analogous to ambient noise in seismology and acoustics.

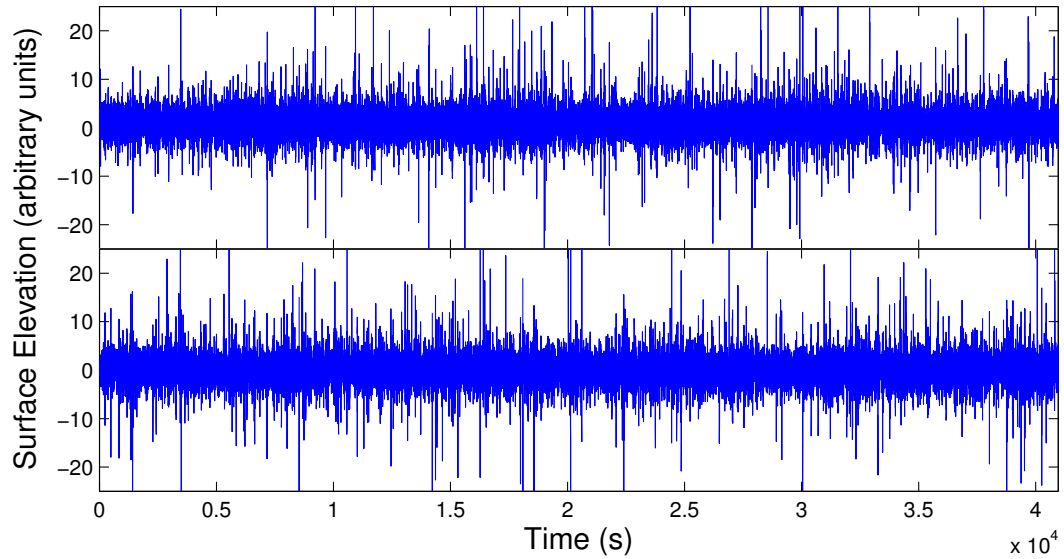


**Figure 4.2:** Simulated time series of surface elevation (40960 s) at  $A$  (upper panel) and  $B$  (lower panel), amplitude units are arbitrary. For viewing purpose, a few measurements with numeric values bigger than 20 are truncated in the plot.

Now we proceed to produce the impulse response between points  $A$  and  $B$ , without losing generality, we excite an impulse at  $A$  and record wave elevations at  $B$ , namely  $A$  is the source and  $B$  is the receiver (the response is the same if  $A$  and  $B$  switch roles). Recall that the distance between  $A$  and  $B$  is 100 m and the group wave speed is 1.56 m/s, the time window for waves generated at  $B$  is about 64 s. This number is later used to decide the cross-correlation time window. Fig 4.3 illustrates the single impulse source excitation response.

Given the single source response time window, we can decide the cross-correlation time window. By definition, cross-correlation is a sliding product between two series.

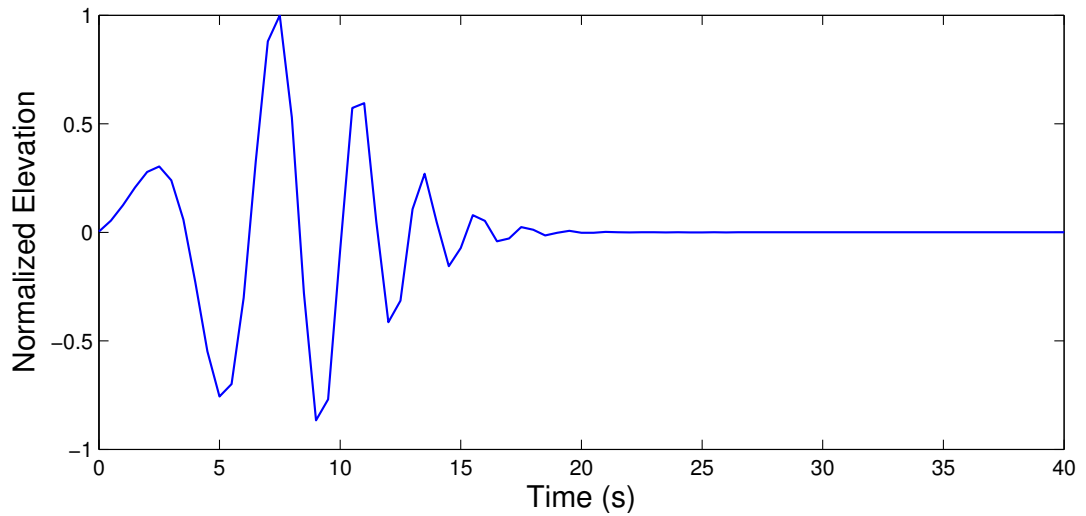


**Figure 4.3:** Surface elevation response  $d(t) * G_{\eta}(\mathbf{x}_B | \mathbf{x}_A, t)$  at  $B$  due to single point source impulsive excitation at  $A$  in the open system. The elevation is normalized to have a maximum value of 1.

Either one of the time sequences is fixed, then the other is slid, for a single run of cross-correlation the fixed sequence should have twice the length of the sliding sequence so that the sliding sequence will not multiply zeros during the run. Based on such considerations, the cross-correlation time window is set to 256 s. The surface elevation time sequence is significantly longer than the cross-correlation window, so we can perform the long-time correlation averaging technique by cross-correlating the shorter subsequences respectively selected from the original sequence. And the time separation between each subsequence is 64 s so that subsequences overlap each other. The final outcome is the grand average of all the subsequences cross-correlation results. Fig.4.4 shows the comparison between the cross-correlation result and GF. It is clear that the cross-correlation is symmetric with respect to the origin, which is a result of propagations between the two receivers in opposite

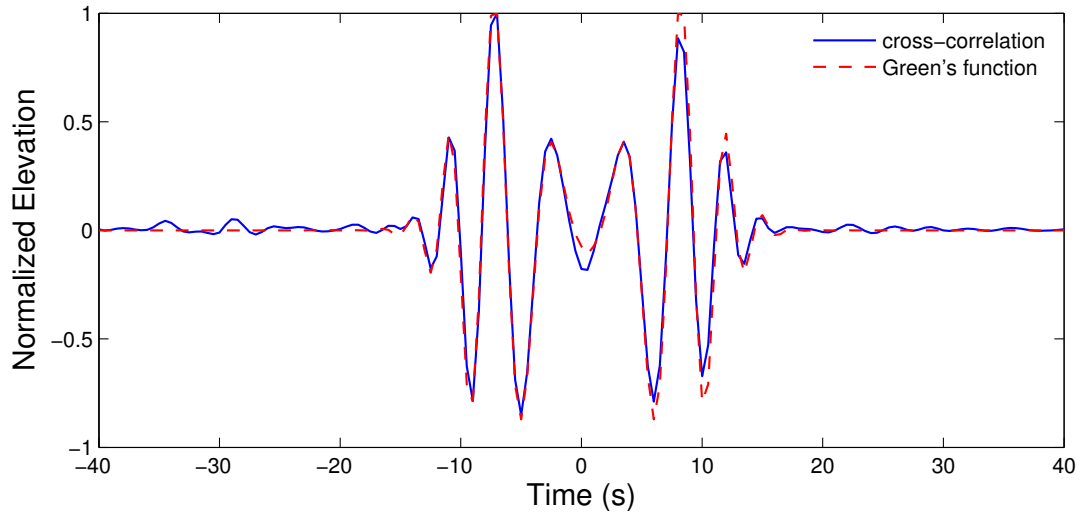


**Figure 4.4:** Cross-correlation  $C_{AB}(t)$  (red dashed curve) of surface elevations  $\eta(\mathbf{x}_A, t)$  and  $\eta(\mathbf{x}_B, t)$  in the open system with deep water dispersion relation, compared to  $D(t) * [G_\eta(\mathbf{x}_B|\mathbf{x}_A, t) + G_\eta(\mathbf{x}_B|\mathbf{x}_A, -t)]$  (blue curve). The cross-correlation is averaged over 6000 realizations. Both curves are normalized to have maximum value of 1.

directions. Note that the red dash curve in Fig.4.4 is not  $d(t) * G_\eta(\mathbf{x}_B|\mathbf{x}_A, t)$  but  $D(t) * [G_\eta(\mathbf{x}_B|\mathbf{x}_A, t) + G_\eta(\mathbf{x}_B|\mathbf{x}_A, -t)]$ , as explained in Chapter 3.

## 4.2 Closed system simulation

For the closed system simulation, we construct the environment as a narrow rectangular wave tank with rigid walls, which is consistent with the closed system theoretical derivation in Chapter 3. Note that besides the environment setup, the closed system simulation is fundamentally different from the open system simulation regarding how the random wave field is generated, and this also reflects the difference in their theoretical derivations. In the open system simulation, we started from the frequency domain where explicit GF is constructed and then transformed into the time domain by taking advantage of the

numerical technique of the inverse Fourier transform. The reason behind such approach is that, in an open system environment, starting from the frequency domain solution is an easier entry point to obtain the eventual time domain series than attempting so directly in the time domain. Switching to a closed system introduces new lateral and vertical boundary conditions, and we are now able to explicitly solve the surface elevation  $\eta$  at any arbitrary location as well as GF via a modal approach, which is done thoroughly with details in Chapter 3.

Recall that a random wave field can be described as a superposition of modes with random phases,

$$\eta(\mathbf{x}, t) = d(t) * \sum_n (c_n \cos \omega_n t + d_n \sin \omega_n t) \psi_n(\mathbf{x}). \quad (4.8)$$

Here  $n$  is the mode number,  $d(t)$  is the band-limited weighting function,  $\psi_n(\mathbf{x})$  is the eigenfunction and random coefficients  $c$  and  $d$  satisfies

$$\langle c_n c_m \rangle = \langle d_n d_m \rangle = a^2 \delta_{nm}, \quad \langle c_n d_m \rangle = 0 \quad (4.9)$$

where  $\langle \rangle$  denotes ensemble average and  $a$  is a constant.

To simulate the random wave field, the above mentioned  $n$ ,  $\psi_n(\mathbf{x})$ ,  $d(t)$ ,  $c$  and  $d$  need to be determined. We start with the mode number  $n$ , normally with the wave tank geometry wave modes are excited in two directions, along the tank and across the tank. Let  $x$  and  $y$  denote position coordinates in the along-tank and cross-tank directions,  $l$  and  $m$  the

corresponding wave numbers and  $L_x$  and  $L_y$  the wave tank length and width. Wave number  $k_{lm}$  is related to the mode numbers by

$$k_{lm}^2 = \left(\frac{l\pi}{L_x}\right)^2 + \left(\frac{m\pi}{L_y}\right)^2, \quad (4.10)$$

And we also have the dispersion relation

$$\omega_{lm}^2 = gk_{lm} \tanh(k_{lm}h), \quad (4.11)$$

where  $h$  is the water depth in the tank. With Eq.4.10 and Eq.4.11 we can numerically decide to what numbers the modes should be excited once the energy bandwidth is determined. Earlier we mentioned that the wave tank is rather narrow, so the receiver locations are chosen along the tank and each is at the center across the tank. In Chapter 2 we learned that the GF estimation is mainly constructed by the cross-correlation of the waves traveling along the receiver axis, this together with the sufficiently narrow wave tank geometry enable us to simplify the system by assuming that only the gravest ( $m = 0$ ) cross-tank mode is excited. There for Eq.4.10 and Eq.4.11 are reduced to

$$k_l^2 = \left(\frac{l\pi}{L_x}\right)^2, \quad (4.12)$$

$$\omega_l^2 = gk_l \tanh(k_l h). \quad (4.13)$$

Now we limit the energy distribution of the simulated wave field to a low frequency band of 0 to 3 Hz. We also set the wave tank parameters as  $L_x = 11.9m$ ,  $L_y = 1m$  and  $h = 0.42m$  (these numbers are so chosen to be consistent with the wave tank experiment in Chapter 6). With Eq.4.12 and Eq.4.13 the range of the lengthwise mode number is computed to be 0 to 140. Note that here  $l$  is essentially equivalent to the mode number  $n$  in Eq.4.8.

For the band-limited weighting function  $d(t)$ , with the bandwidth being  $0 < f < 3$  Hz, it is reasonable to set the peak frequency to 1.5 Hz. To modulate the energy distribution in the frequency domain, we assume  $\bar{d}(\omega)$  has the form

$$\bar{d}(\omega) = \begin{cases} 3\omega\pi e^{-\omega/3\pi}, & \text{for } \omega < 3\pi \\ \omega^2 e^{-(\omega/3\pi)^2}, & \text{for } \omega \geq 3\pi \end{cases} \quad (4.14)$$

Note that since every mode number corresponds to a specific frequency in the frequency domain, it is rather simpler to compute the weight coefficient regarding each frequency and apply onto the corresponding mode than to convert Eq.4.14 to time series and then do the convolution in time domain.

The eigenfunction function  $\psi_{lm}(\mathbf{x}) = \cos(l\pi x/L_x)\cos(m\pi y/L_y)$  is also reduced to  $\psi_l(\mathbf{x}) = \cos(l\pi x/L_x)$  because of  $m = 0$ . And coefficients  $c$  and  $d$  are generated via Box-Muller transform using the following formula:

$$\begin{aligned} c &= \sqrt{-2 \ln U_1} \cos(2\pi U_2), \\ d &= \sqrt{-2 \ln U_1} \sin(2\pi U_2) \end{aligned} \quad (4.15)$$

where  $U_1$  and  $U_2$  are independent random variables that are uniformly distributed in the interval  $(0, 1)$ .

With all the components determined, a random band-limited waver field can be numerically simulated as a special case of Eq.4.8,

$$\eta(\mathbf{x}, t) = d(t) * \sum_l (c_l \cos \omega_l t + d_l \sin \omega_l t) \cos\left(\frac{l\pi x}{L_x}\right). \quad (4.16)$$

The two receivers are located at  $A(2.38m, 0.5m)$  and  $B(9.52m, 0.5m)$ . Fig.4.5 shows wave field surface elevation simulated for 5 hours with sampling frequency  $f_s = 50$  Hz.

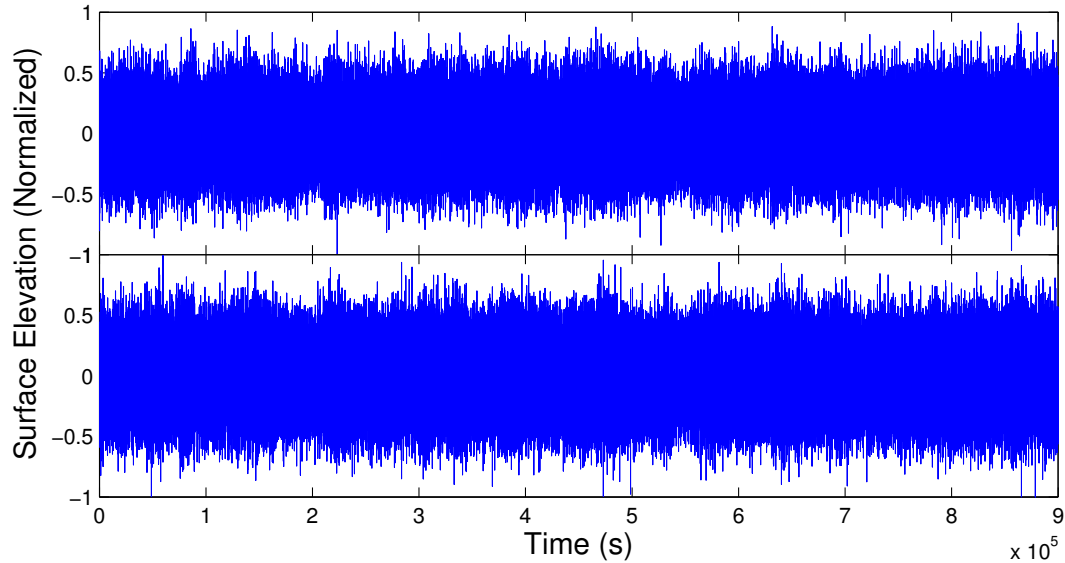


**Figure 4.5:** 5 hour time series of simulated random surface elevation  $\eta(\mathbf{x}_A, t)$  (upper panel) and  $\eta(\mathbf{x}_B, t)$  (lower panel) in the wave tank geometry. Both curves are normalized to have a maximum value of 1.

Similarly with the wave tank geometry GF in the time domain is also computed explicitly in Chapter 2,

$$G_\eta(\mathbf{x}_B|\mathbf{x}_A, t) = \frac{1}{L_x L_y} H(t) \sum_l \sum_m \beta_l \beta_m \psi_{lm}(\mathbf{x}_A) \psi_{lm}(\mathbf{x}_B) \cos \omega_{lm} t, \quad (4.17)$$

where  $H(t)$  is the Heaviside step function and  $\beta_l = 1$  for  $l = 0$ ,  $\beta_l = 2$  for  $l = 1, 2, \dots$

Again we simplify Eq.4.17 by assuming  $m = 0$ :

$$G_\eta(\mathbf{x}_B|\mathbf{x}_A, t) = \frac{1}{L_x L_y} H(t) \sum_l \sum_m \beta_l \cos\left(\frac{l\pi x_A}{L_x}\right) \cos\left(\frac{l\pi x_B}{L_x}\right) \cos \omega_l t, \quad (4.18)$$

Now before we can simulate the GF signal between  $A$  and  $B$ , a time window needs to be calculated in a similar fashion as in the open system simulation. However, with the wave tank geometry we no longer assume deep water condition, instead the general dispersion relation (Eq.4.11) is now considered. Phase speed  $c_p$  can be computed by,

$$c_p = \omega/k \quad (4.19)$$

Substituting  $\omega$  from Eq.4.11 into Eq.4.19 and assuming  $m = 0$ , we get the phase speed as a function of  $k_l$ ,

$$c_p = \sqrt{\frac{g}{k_l} \tanh(k_l h)}, \quad (4.20)$$

and we already know that  $k_l = l\pi/L_x$  (Eq.4.12) and  $0 \leq l \leq 140$ . Numerically the minimum of the phase speed is computed to be 0.27 m/s. We know in shallow water the

group speed is equal to the phase speed, and in deep water the group speed is half the phase speed, since we seek a minimum group speed for the purpose of a minimum time window, it is reasonable to assume the group speed to be half of the phase speed, namely 0.14 m/s, even though we do not assume either shallow or deep water condition. And with

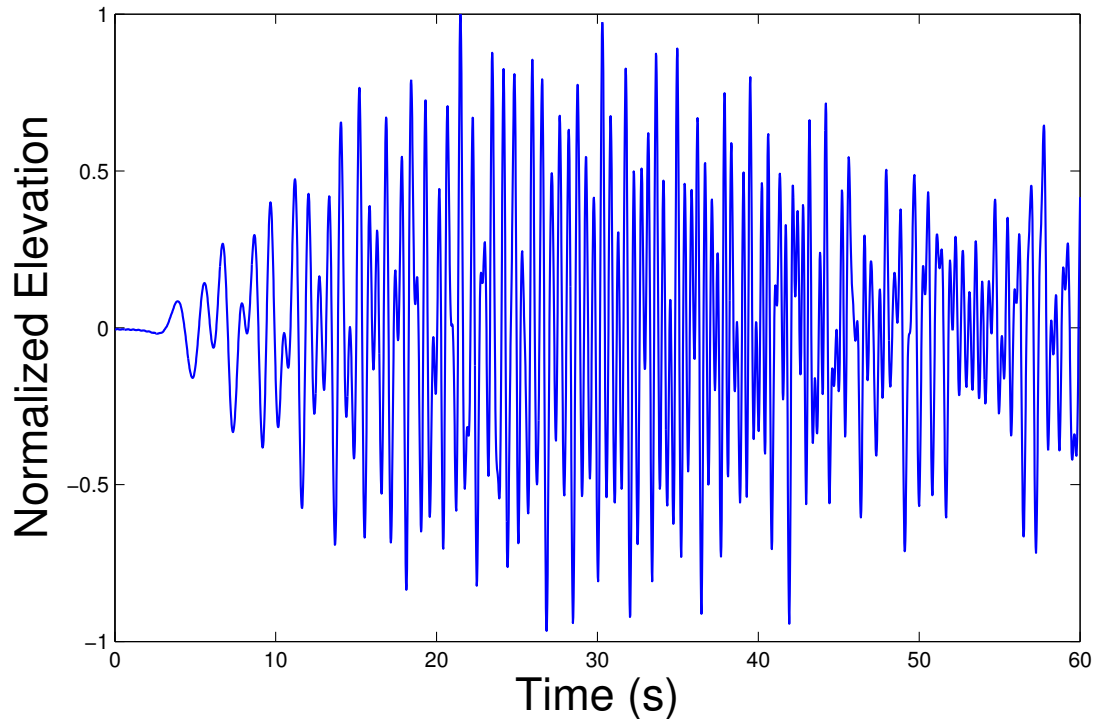


**Figure 4.6:** Simulated surface elevation response  $d(t) * G_\eta(\mathbf{x}_B|\mathbf{x}_A, t)$  computed based on Eq.3.35 in the wave tank geometry. The curve is normalized to have a maximum value of 1.

the distance between  $A$  and  $B$  being 7.14 m, the time window therefore should be at least 51 s. For convenience, we set the time window to be 60 s. Fig.4.6 shows the simulated surface elevation GF response.

Now we move onto cross-correlating the simulated random wave field surface elevations. The procedure is almost identical to how it is done in the open system simulation. The cross-correlation result time window is two times the individual response time window

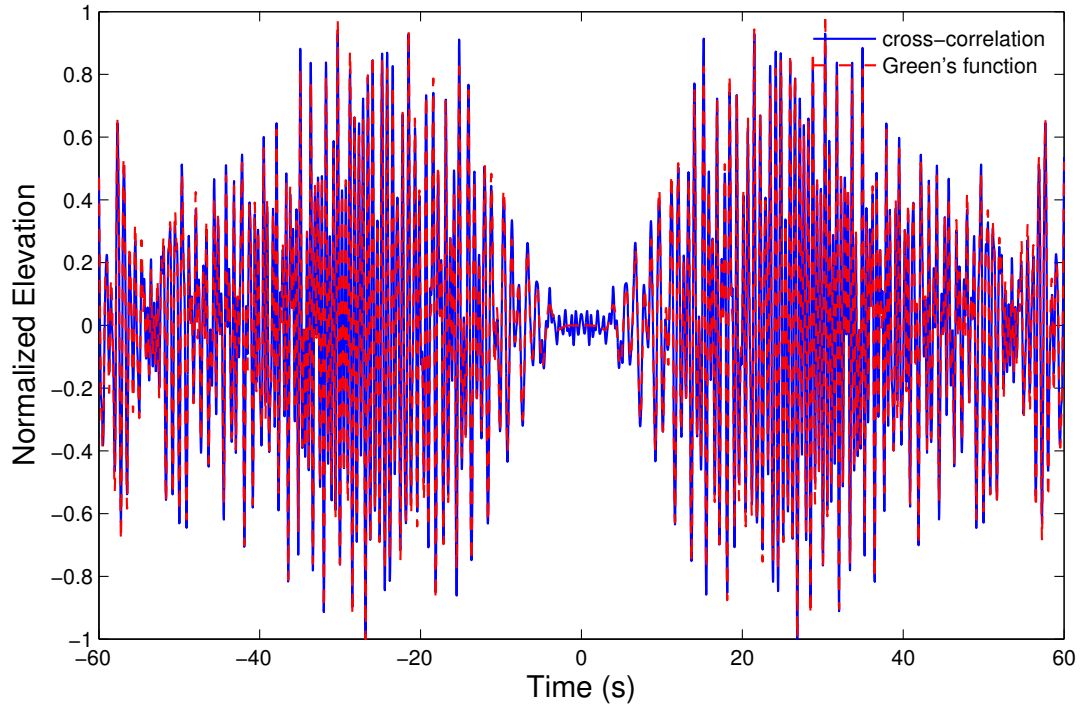


**Figure 4.7:** Cross-correlation  $C_{AB}(t)$  (blue curve) of random surface elevation  $\eta(\mathbf{x}_A, t)$  and  $\eta(\mathbf{x}_B, t)$  in the wave tank geometry, compared to  $D(t) * [G_\eta(\mathbf{x}_B|\mathbf{x}_A, t) + G_\eta(\mathbf{x}_B|\mathbf{x}_A, -t)]$ . The cross-correlation is averaged over 240 realizations. Both curves are normalized to have a maximum absolute amplitude of 1.

(60 s), namely 120 s. So for each subsequence pairs, the fixed subsequence is 240 s long and the sliding subsequence is 120 s long. Earlier we simulated the random wave field surface elevation for 5 hours, now we pick subsequences from the two time series incrementally with a separation of 20 s and perform cross-correlation with each subsequences pairs. Fig.4.7 shows the averaged cross-correlation result  $C_{AB}(t)$  versus  $D(t) * [G_\eta(\mathbf{x}_B|\mathbf{x}_A, t) + G_\eta(\mathbf{x}_B|\mathbf{x}_A, -t)]$ .

From Fig.4.7 we can see that the cross-correlation matches the GF very well. Since the cross-correlation is very much symmetric, we flip the part of the negative delay, add to the positive side and average again. Fig.4.8 shows the comparison between one-sided

cross-correlation and  $D(t) * G_\eta(\mathbf{x}_B|\mathbf{x}_A, t)$ . The two curves have a correlation coefficient of 0.99.

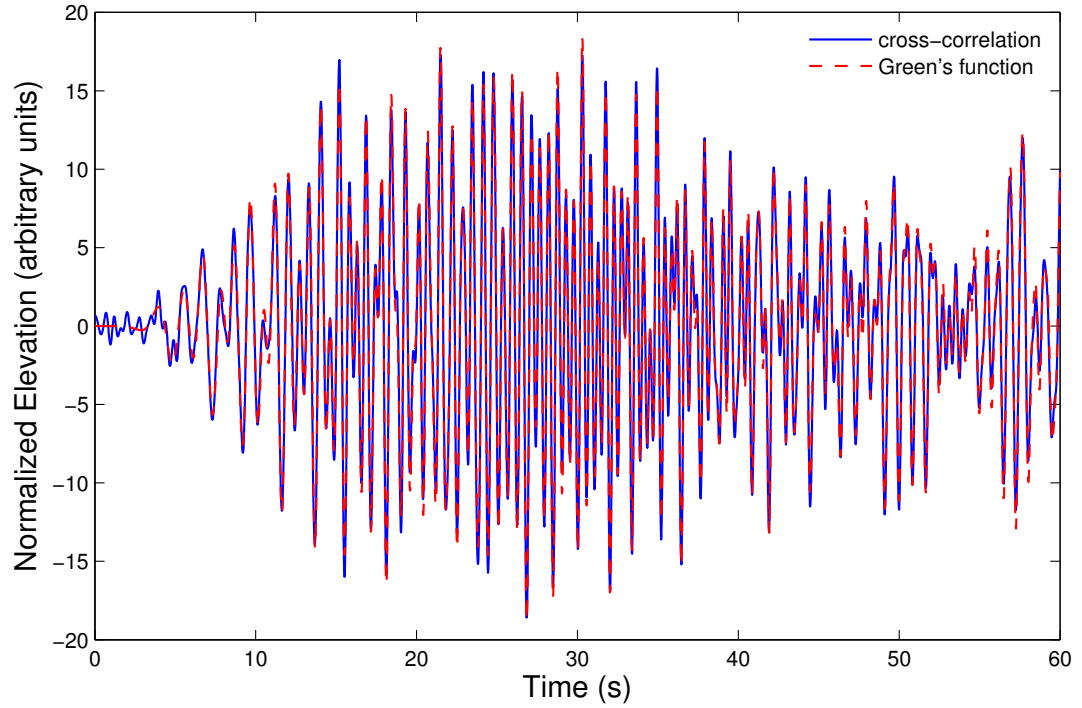


**Figure 4.8:** Cross-correlation  $(C_{AB}(t) + C_{AB}(-t))/2$  (blue curve) of random surface elevations  $\eta(\mathbf{x}_A, t)$  and  $\eta(\mathbf{x}_B, t)$  in the wave tank geometry, compared to  $D(t) * G_\eta(\mathbf{x}_B|\mathbf{x}_A, t)$ . The cross-correlation is averaged over 240 realizations. Both curves are normalized to have a maximum absolute amplitude of 1.

# Chapter 5

## Field Experiment Data Analysis

In Chapter 4 we simulated the GF retrieval via cross-correlation in an open system and the result is very promising. In this chapter we aim to analyze wave heights data collected during two field experiments and attempt to estimate GF via cross-correlating relevant surface elevation records. While the intention of this chapter is to further validate the theoretical proof in Chapter 3 regarding the open ocean geometry, the actual correlation results do not seem to provide good GF estimations. Nevertheless, by studying the various aspects of the field experiments we obtain valuable insights on GF retrieval in the open ocean field. Chapter 7 also gives possible reasons and explanations regarding the data analysis result. Section 5.1 presents the FETCH experiment and Section 5.2 focus on the SW06 experiment.

## 5.1 FETCH experiment

As one of the major field experiments on momentum and energy exchange near the air/sea interface in the last several decades, FETCH ("Flux, Etat de la mer, et Tldtection en Conditions de fetch variable") was an international field campaign organized by French, American and Finnish groups in 1998 in the northwestern Mediterranean Sea (Gulf of Lyon). The field experiment was designed to study the physics of air-sea interactions, and wave growth in a coastal region of strong offshore wind dominance during the time period of March 12 to April 16 1998 [30, 23, 12, 13]. The field data collected during FETCH was a rich combination of measurements using various instruments including a ship, buoys, aircrafts and satellites [30]. The wave heights data we are most interested in regarding GF retrieval was measured by the Air-Sea Interaction Spar (ASIS) and Directional Waverider (DWR) buoys. ASIS and DWR buoys were deployed at  $42^{\circ}58'56''N$ ,  $04^{\circ}15'11''E$ , approximately 60 km from the shore (point  $B$  in Fig.5.1) with a distance of about 2 km in between. DWR and ASIS were moored on March 16 and March 18 respectively and the water depth of the mooring site was 100 m (deep water condition). On March 25, DWR was recovered and redeployed at  $43^{\circ}09'34''N$ ,  $04^{\circ}06'15''E$ , 25 km north-northwest from ASIS (point  $B'$  in Fig.5.1).

Before we look into the details of the datasets, it is helpful to understand how the wave heights are measured by the buoys. For ASIS, the surface elevation was measured by an array of capacitance wave gauges which were installed in the pentagonal cage of slender cylinders together with a central spar element. Five of the six gauges were mounted

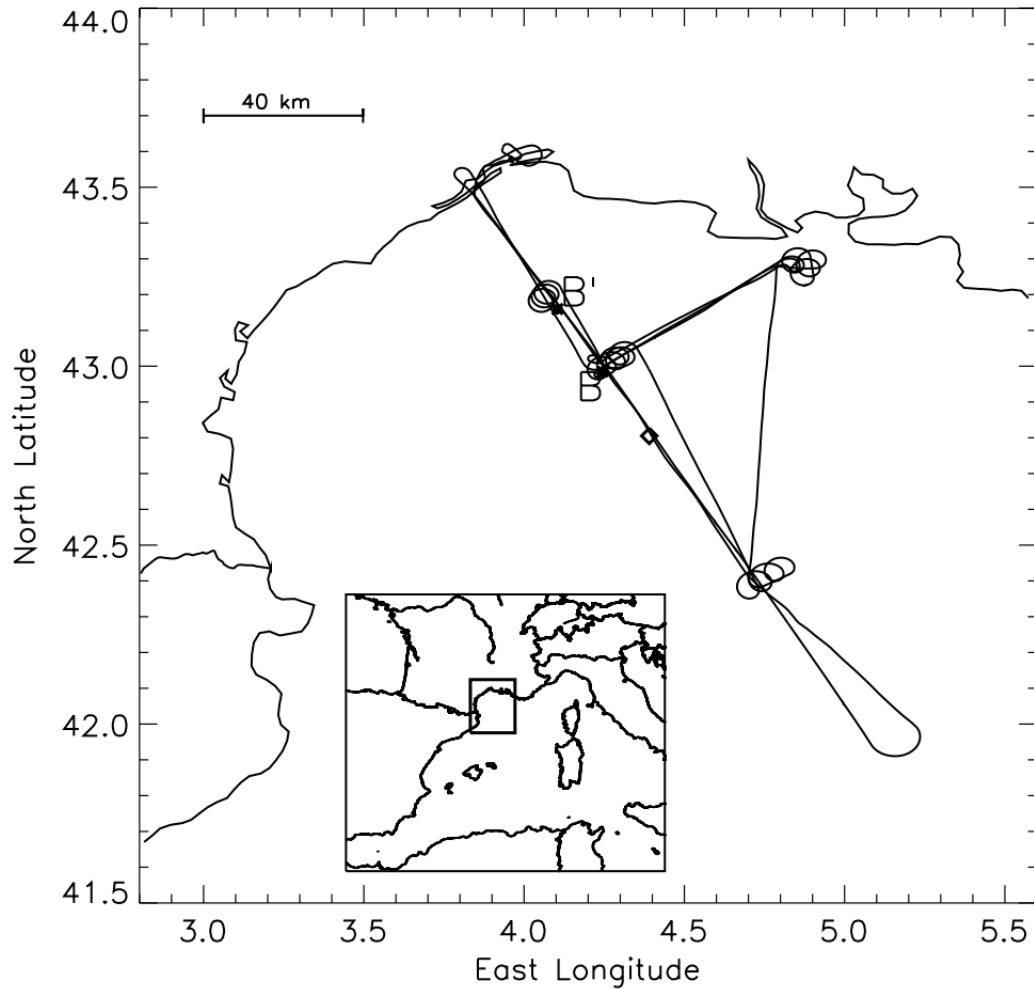


**Figure 5.1:** Geographic map of the FETCH experiment. Point B is the location of the ASIS buoy from 18 March to 9 April. DWR was also at this location from 16 March to 25 March. Point B' is the location of DWR after 25 March. Adapted from "Directional wave measurements from three wave sensors during the FETCH experiment" by Pettersson, Heidi. *Journal of Geophysical Research*, 108(C3), 2003.

along the perimeter of a pentagon of 92.7 cm radius, and a sixth was mounted at the center. ASIS was able to resolve waves of lengths greater than about 2 m. During the first half of the experiment (March 1998) one of the wave gauges was broken, and all were operational during the second half of the experiment in April. DWR does not measure surface displacements directly, instead as a spherical buoy it follows the water surface

and measures the three components (vertical, pitch and roll) of linear acceleration with accelerometers fixed to its hull. These measurements together are then integrated to yield surface displacements. Based on the dimensions of DWR, its highest measurable frequency is 0.6 Hz. Notice that DWR was not equipped with a data logging system, and therefore had to transmit the data to the nearby research ship. Since the ship was not always in the reception range, the time series were only received for about half of the time [30].

With those facts of the wave sensors in mind, we need to address several issues of the wave heights data before cross-correlation. First, the ASIS data were processed in blocks of 28.5 minutes with a roughly 1 minute pause between each block and similarly the DWR data were processed in blocks of 20 minutes separated by 10 minutes pauses. No surface displacements were recorded during those pauses and the corresponding phase information, which are crucial to correlation, were therefore cut off. The existence of these long halts invalidates the idea of having two continuous data sequences respectively for ASIS and DWR as long time wave trains at two locations. With the gaps in the surface elevation measurements, cross-correlation has to be done with short individual ASIS and DWR data block pairs. Second, the sampling frequencies of these two buoys were different: 12 Hz for ASIS and 1.28 Hz for DWR. In order to synchronize the data points, we resample the ASIS data at 1.28 Hz so that the ASIS and DWR data blocks have the same frequency therefore the same number of discrete sampling data points for each correlation. Third, as mentioned in the previous paragraph DWR had no internal data logging equipment and it transmitted measurements to a receiver on board the research ship during the FTECH experiment. This

caused some serious problems when the ship was far from the DWR buoy or the sea conditions were rough, while some of the data blocks were lost during transmission some of the received data blocks contained obviously false wave height values that were unreasonably large. These problems set further criteria to the selection of the DWR data blocks for correlation. In order to eliminate the potential errors caused of data loss and false measurements, we pick a group of DWR data blocks, which are successive in time and do not contain false wave heights, and then find the time-wise corresponding sections from the resampled ASIS data to perform cross-correlation. To increase the signal-to-noise ratio, multiple correlations by different data block pairs are averaged. Therefore a DWR data group that has more successive blocks has higher priority to be considered for correlation. Finally, the FETCH experiment was originally aimed at studying the air-sea interactions in high wind conditions, so it was held within a chosen time period of high offshore winds. This is indeed a major disadvantage for our research purpose because GF retrieval via cross-correlation favors a random wave field instead of a wind-dominated wave field. For this reason, we decide not to use data obtained after March 24 due to the largely extended distance between the two buoys, which intensified the effects of the wind dominance and significantly weakened the randomness of the field. In order to alleviate the wind dominance as much as possible, we refer to the wind speed profile during FETCH (Fig.5.2) and choose a time period when the wind speed is relatively low (below 3 m/s) and use the data collected during that period for cross-correlation.

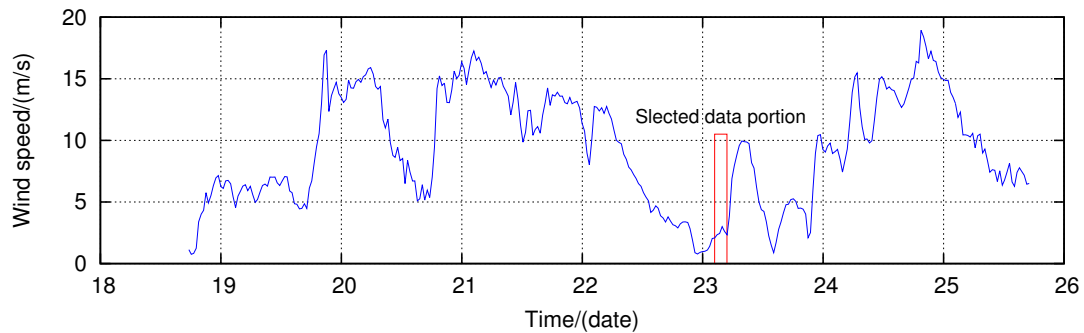


**Figure 5.2:** Wind speed measured by ASIS buoy from March 18 to March 26 during the FETCH experiment. The time period highlighted by the red box has relatively low wind speed and is therefore selected for cross-correlation. The time axis is day in the month of March.

Based on all the considerations above, we pick two groups respectively from ASIS (after resampling) and DWR data from 02:20 to 05:00 on March 23 which is highlighted in Fig.5.2. Fig.5.3 shows the time series of the selected data chunk from ASIS and DWR.

According to Pettersson [30], the peak frequency of the surface waves is about 0.15 Hz and the ASIS and DWR data agree with each other on this measurement. We are most interested in the waves confined in the bandwidth of 0 to 0.3 Hz (with the high end being twice of the peak frequency). Under deep water condition, we compute the minimum phase speed using Eq.4.5 with the cutoff frequency (0.3 Hz), which yields 5.2 m/s. In deep water the group speed is half the phase speed, therefore  $c_g = 2.6$  m/s. And the distance between ASIS and DWR is 2 km, so the maximum time delay is about 12.8 minutes. Since the gaps in ASIS data is much shorter than those in the DWR data, we use the ASIS data as the fixed sequence and the DWR data as the sliding part. Usually we set the sliding window to be twice the computed maximum time delay and slide left and right half of the sliding window, so the subsequence should be 25.6 minutes in this case. However, 25.6 minutes

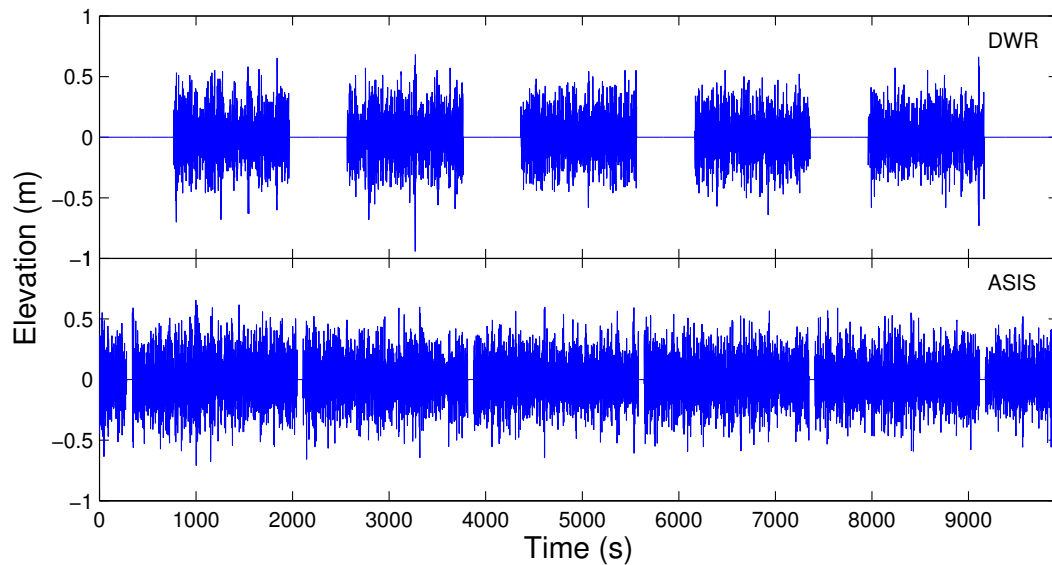


**Figure 5.3:** Surface elevation data measured by DWR (upper panel) and ASIS (lower panel) from 02:20 to 05:00 on March 23. 10 minute gaps appear every 20 minutes in DWR data and 1 minute gaps appear every 29 minutes in ASIS data. ASIS data are resampled and synchronized with DWR data. The time axis is the total time of the selected data in seconds.

exceeds the length of each block in the DWR data, so the cross-correlation is a little bit different from the simulation: we set the sliding time window to be 12.8 minutes long and the fixed window 3 times the length with originally their window centers aligned at the same time stamp, and then slide from left to right. The sliding distance is still twice the lag time and both negative and positive time delays are covered. Because of the 10 minutes gap in DWR data, we process each block using the same technique as in the simulations and then average again over all blocks. The time separation between each subsequence is 30 s. Fig.5.4 shows the final cross-correlation result averaged over all groups. With peak frequency being 0.15 Hz, the dominant wave travels at group speed 5.2 m/s, so we expect the envelope to reach maximum around time delay  $t = \pm 6.4$  minutes (384 s). We can see

in Fig.5.4 that the correlation result does not give any sign of deterministic structure, and possible reasons will be discussed in Chapter 7.

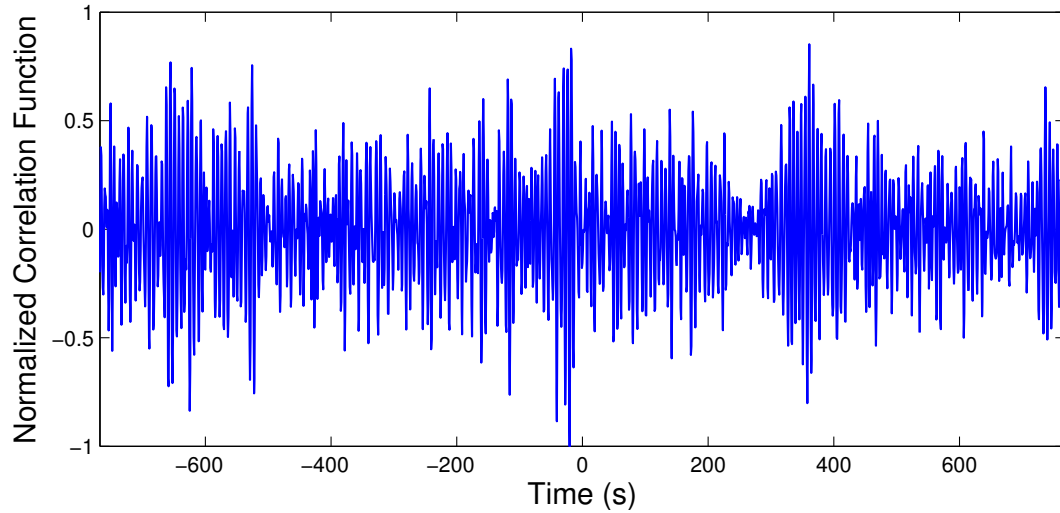


**Figure 5.4:** Cross-correlation  $C_{AB}(t)$  of surface elevation  $\eta(\mathbf{x}_A, t)$  and  $\eta(\mathbf{x}_B, t)$  measured in FETCH experiment. The cross-correlation is averaged over 75 realizations and normalized to have maximum absolute value of 1.

## 5.2 SW06 experiment

The second dataset we tried to make use of are collected during the Shallow Water '06 experiment (SW06). SW06 was a large, multi-institution, multidisciplinary, multinational field experiment on the continental shelf offshore New Jersey from July to September 2006. The large-scale project was composed of three major research topics: acoustics, physical oceanography, and vehicles[55, 29, 27, 31]. Similar to FETCH, measurements in SW06 involved a great variety of instruments including ships, mooring, aircrafts and satellites. And the wave heights measurements we consider for our purpose were those recorded by two ASIS buoys named Romeo and Yankee, they were deployed to provide

local air-sea interaction observations as part of the Non-Linear Internal Wave Initiative (NLIWI) program. Romeo was located at  $39.0739^{\circ}\text{N}$ ,  $73.1641^{\circ}\text{W}$  and Yankee was located at  $39.0192^{\circ}\text{N}$ ,  $73.0536^{\circ}\text{W}$ . They were deployed with a distance of 11.33 km between each other and their mooring sites have very similar water depth: Romeo at 71 m and Yankee at 77 m (both satisfies deep water condition). Both of the buoys were deployed from July 29 to September 15 2006. Fig.5.5 shows the locations of Romeo and Yankee.

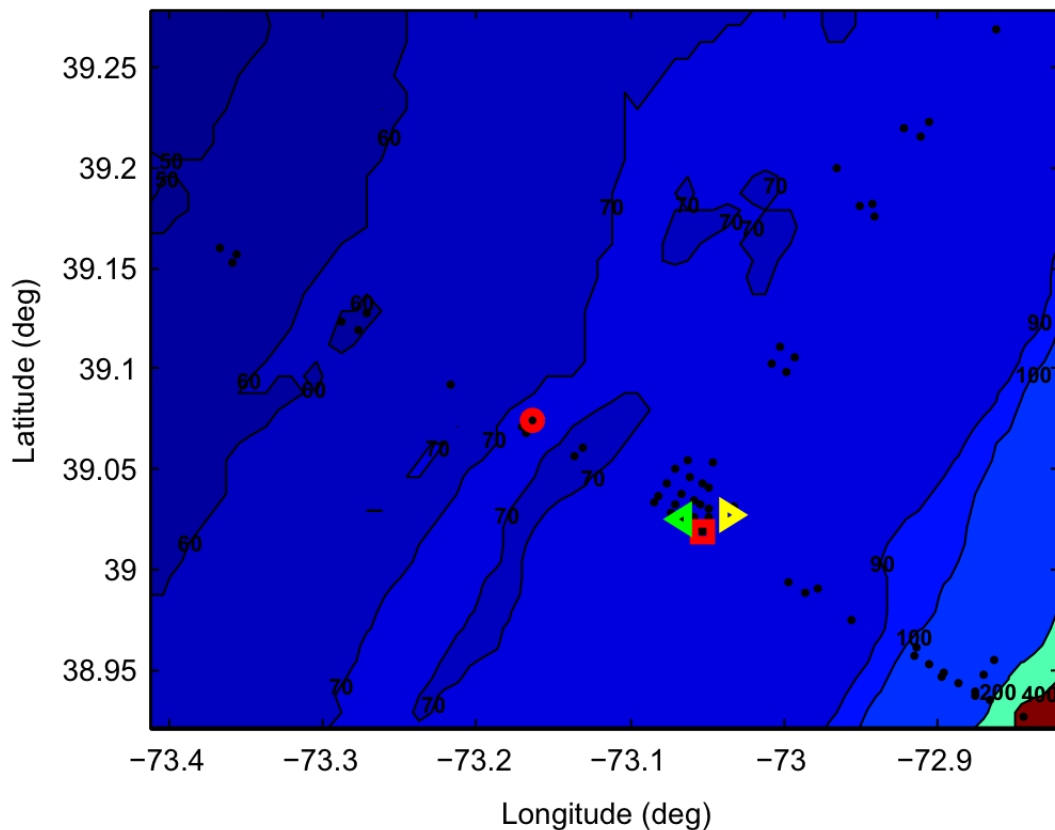


**Figure 5.5:** Geographic map of the ASIS buoys during SW06 experiment. Red circle indicates the location of Romeo and red square indicates the location of Yankee. Adapted from "Determination of internal wave properties from X-Band radar observations" by Ramos, Rafael J., Lund, Björn and Graber, Hans C. *Ocean Engineering*, 36(14):1039-1047, 2009.

Compared to FETCH data, SW06 datasets have a couple of improvements. First, Romeo and Yankee are both ASIS buoys, so their measuring systems are identical while one FETCH buoy was ASIS and the other was DWR. This provided better consistency with the surface elevation measurements. Issues such as transmitting data from mooring site to ships no longer existed. Another advantage is that Romeo and Yankee shared the same sampling frequency of 20 Hz (since a sample rate of 20 Hz is actually more than enough for our research purpose, we resample both the Romeo and Yankee data at 10 Hz to simplify the datasets). Second, the integrity of SW06 data is much better compared to that of FETCH data. While data loss still existed during SW06, the data loss ratio is significantly lower compared that of FETCH. Both the Romeo and Yankee data had on average 1 minute data loss per hour, for about ten days' recording. With this data loss ratio we can fill the data gap with zeros and perform the long-time average cross-correlation technique as in the simulation, expecting that averaging over many subsequence cross-correlation results compensates the weak "noise" caused by the low-ratio data loss. Despite the above mentioned advantages SW06 had over FETCH, one potential downside about the SW06 data is that Romeo and Yankee were deployed 11.33 km away from each other. This separation is much larger than the 2 km distance of FETCH buoys, and could potentially contribute to local wave development. The available wave heights data lasts around 10 days. Although SW06 was not intended for air-sea interaction studies, the wind speed profile (Fig.5.6) during SW06 shows that high winds existed for the majority of the 10-day time period. Based on the same consideration as with FETCH data, we select a portion of

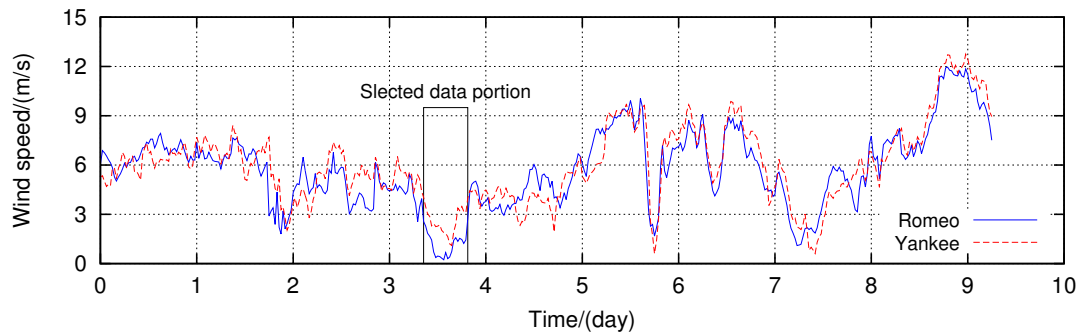


**Figure 5.6:** Wind speed measured by Romeo (blue curve) and Yankee (red curve) from August 2 to August 11 during the SW06 experiment. The time period highlighted by the black box has relatively low wind speed and is therefore selected for cross-correlation. The time axis is the total time in days.

the data that was recorded under relatively low speed wind to reduce the wind influence.

The vertical box in Fig.5.6 indicates the selected data portion from 21:59:00 on August 5, 2006 to 09:11:00 on August 6, 2006. And Fig.5.7 shows the resampled surface elevation time sequences during the selected time period. The total time length a bit over 11 hours.

Power density spectrum analysis of the SW06 data sequences yields a peak frequency of 0.35 Hz, and we pick 0.5 Hz as the cutoff frequency, which leads to a minimum phase speed of 3.12 m/s (based on Eq.4.5). Again the deep water condition is satisfied, therefore the minimum group speed is half the minimum phase speed, 1.56 m/s. Recall the distance between Romeo and Yankee is 11.33 km, so the longest time delay for a surface wave to travel from Romeo to Yankee is around 120 minutes. The cross-correlation window should cover both the negative and positive delays, so we set it to be 240 minutes (4 hours). Therefore the sliding subsequence is 4 hours long and the fixed subsequence is 8 hours long. Unlike the large gaps of the DWR data in FETCH, Romeo and Yankee both have short data loss, so either of them can be the sliding or fixed subsequence. We also set the separation

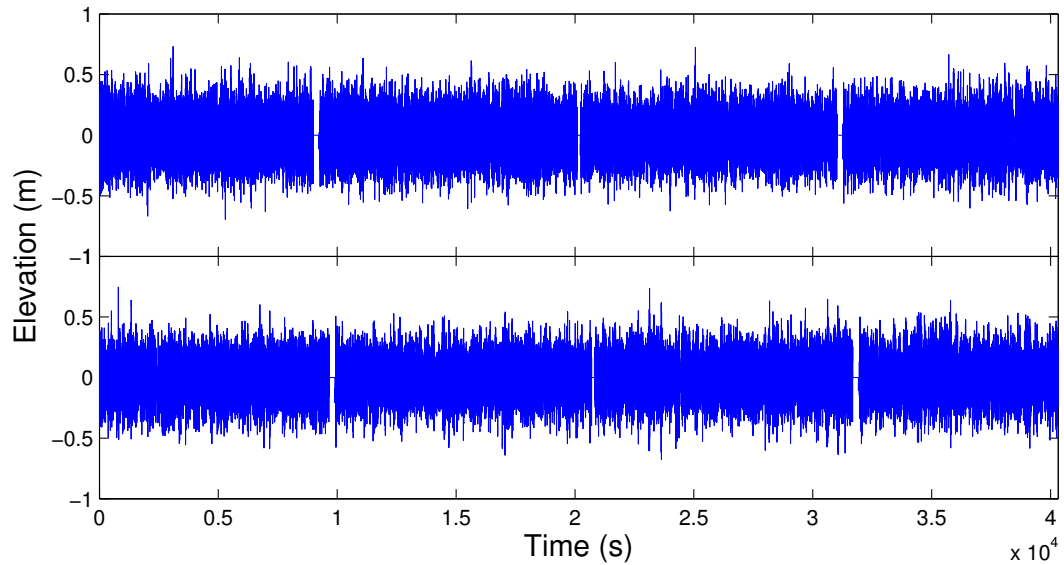


**Figure 5.7:** Surface elevation data measured by Romeo (upper panel) and Yankee (lower panel) from 21:59:00 on August 5, 2006 to 09:11:00 on August 6, 2006. On average 1 minute gaps appear very hour in both Romeo and Yankee data. The time axis is the total time of the selected data in seconds.

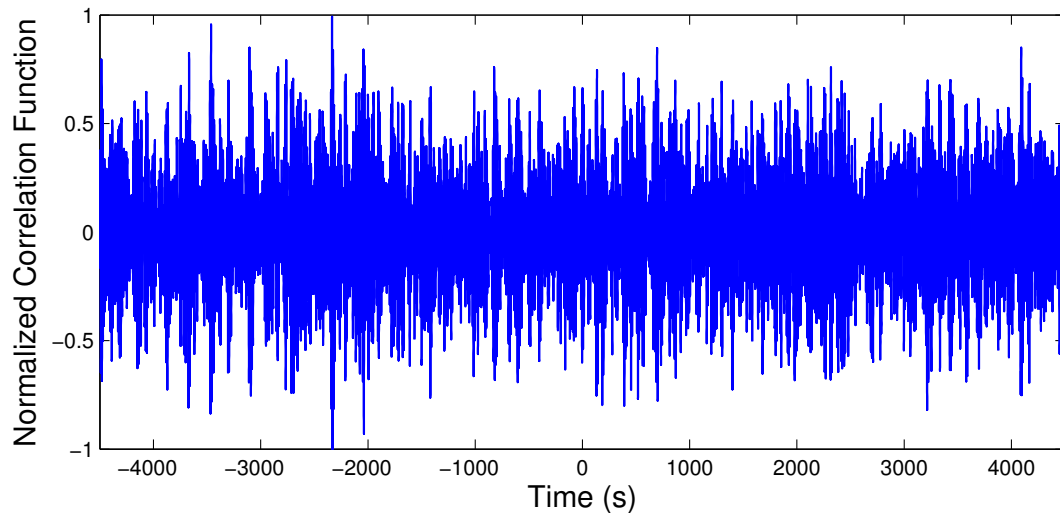


**Figure 5.8:** The cross-correlation  $C_{AB}(t)$  of surface elevation  $\eta(\mathbf{x}_A, t)$  and  $\eta(\mathbf{x}_B, t)$  measured in SW06 experiment. The cross-correlation is averaged over 16 realizations and normalized to have maximum absolute value of 1.

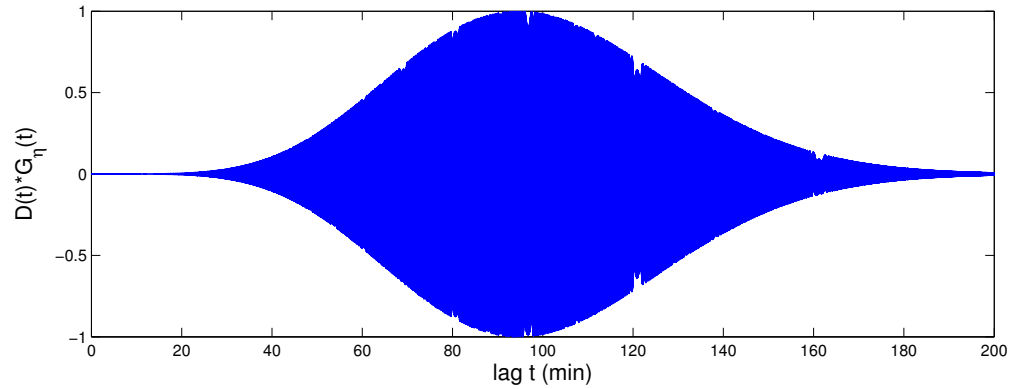


**Figure 5.9:** Simulated GF  $D(t) * G_{\eta}(t)$  based on the geometry in SW06 experiment. GF is normalized to have a maximum absolute value of 1.

between each separation to be 5 minutes, which means the cross-correlation is averaged over 40 iterations. Fig.5.8 is a plot of the averaged cross-correlation result. Peak frequency of 0.35 Hz leads to a group speed of 2.23 m/s, and with the distance of 11.33 km GF is expected to have peak envelop around  $t = 84.7$  minutes, as suggested by the simulated SW06 GF in Fig.5.9. With the improvements of the SW06 datasets we expected a better result than that with the FETCH datasets, however, no sign of deterministic structure is shown in Fig.5.8, and potential causes are discussed in Chapter 7.

# Chapter 6

## Wave Tank Experiment

In Chapter 4 we presented two sets of numerical simulation to support each of their theoretical derivations, and in the previous chapter we specifically studied the surface wave elevation data in two field experiments attempting to support the open ocean simulation. Unfortunately, neither of the field experiment data is able to produce a good estimation of the GF response. One of the reasons is those experiments were not dedicated for our research purpose, instead the only available surface elevation measurements were in fact particularly designed for air-sea interactions studies. We are aware that many conditions and parameters were not favored by us, therefore a field experiment with considerations of our research purpose would be ideal. However, for practical and economical reasons, a small scale experiment with well controlled conditions and parameters turns out to be a better choice. Besides, a wave tank experiment is the right component for the integrity of this thesis work. Therefore, in this chapter, we complete the research topic by performing

an indoor wave tank experiment that is deliberately tailored to realize the closed system simulation.

## **6.1 The wave tank facility**

The wave tank facility used in this experiment is the Air-Sea Interaction Salt water Tank (ASIST). ASIST is a unique and versatile facility that is able to create surface waves in a controlled closed environment. Scientists and researchers of various interests have used ASIST to reproduce on a small-scale phenomena like the high winds in hurricanes, breaking waves and rogue waves and their impact on the ocean, man-made structures, and natural environments like beaches and coral reefs. Additionally, the laboratory benefits from advanced measurement technology such as particle velocimetry, which provides non-intrusive mean flow and turbulence measurements with high resolution in both space and time. ASIST also has the capacity to make C-band Doppler radar measurements, hot film anemometry for turbulence observations, infrared surface temperature observations and to measure CO<sub>2</sub> and water vapor transfer rates. Fig.6.1 is a picture of ASIST.

As its name suggests, ASIST mainly focused on research of air-water interactions with a fan that can create winds with speeds from 0 to 30 m/s and a pump for generating currents up to 0.50 m/s. The laboratory enables measurements that are difficult or impossible to make in the open ocean. ASIST is also equipped with a fully programmable wave maker that are able to generate surface gravity waves of different amplitudes and frequencies based on the input signal. The wave tank, specially built with stainless steel and acrylic to



**Figure 6.1:** A photograph of Air-Sea Interaction Salt water Tank (ASIST). Photograph is taken from the tank head in the along tank direction. Water is not filled in the tank at the time.

resist salt water, is 15 meters long, 1 meter high and 1 meter wide. Fig.6.2[37] shows the view inside ASIST.

## 6.2 Experiment procedure

ASIST is equipped with programmable wave maker and advanced measurement instruments, so the experiment procedure is very straightforward: generate random wave field and record surface elevation.

ASIST has two separate wave generating systems, one is fan and the other is wave maker. Fan is primarily used to reproduce wind generated waves, wave maker can generate



**Figure 6.2:** View from inside Air-Sea Interaction Salt water Tank (ASIST). Water in the tank is colored with green dye.

stabler swell waves. Because our GF retrieval approach is supposed to work in a random wave field where the waves are well developed swells, it is apparent that we use wave maker as a source to generate waves. The wave maker drives a hydraulic piston to move back and forth and therefore creates waves. A rectangular steel panel is placed at the end of ASIST, and vertically aligned with the cross-section of the tank. The back of the panel is welded to the hydraulic piston driven by the wave maker. When signals are fed to the wave maker, the steel panel, dragged by the hydraulic piston, makes horizontal motions along the tank and pushes the water body to create waves. We generate a bandwidth-limited digital time signal of random phases using Matlab and then use a digital-to-analog signal

converter to convert the digital signal to an analog signal, which is then fed to the wave maker. The discrete pseudo-random time signal is created by performing the inverse FFT to a frequency domain function that has the exact same shape as the weighting function (Eq.4.14) in the closed system simulation with extra random phase (uniformly distributed between 0 and  $2\pi$ ) added. Also same as in the simulation, the peak frequency is 1.5 Hz and most of the energy is confined in the bandwidth of  $0 < f < 3$  Hz. And the sampling frequency is 20 Hz. One iteration of the inverse FFT generates a time series of 204.8 s, and the same procedure is repeated 88 times to create a 5 hour long time sequence to supply to the wave maker for the duration of the experiment. The wave maker runs about 10 minutes before recording starts so that waves are stable. Fig.6.3 [9] is a schematic of ASIST, which shows the structure of ASIST.

The parameters of the wave tank experiment are identical as those in the simulation. There is an aluminum slope at the tail of ASIST that is used to emulate ocean beach. We installed a vertical wooden wall in front of the beach; the effective tank length was measured to be 11.9 m, also the same as in the simulation. The hydrostatic water depth is 42 cm. The recording locations are 2.50 m (*A*) and 9.39 m (*B*) away from the tank head along the tank and centered across the tank. The surface elevation measuring system equipped with ASIST is very different from ordinary surface elevation gauges. It consists of laser illuminators and high speed line-scan cameras. Laser illuminators shoot laser beams through the water body vertically at the recording locations from the bottom of the tank.

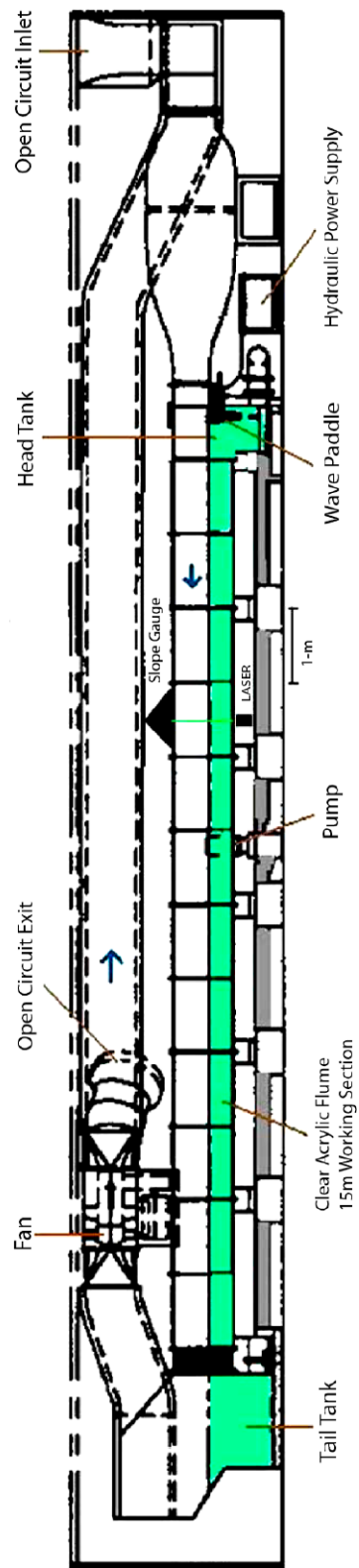


**Figure 6.3:** A schematic of Air-Sea Interaction Salt water Tank (ASIST)

The water in the tank is colored with green dye and the water line is brightened by the laser beam traveling along it, as shown in Fig.6.4[38].

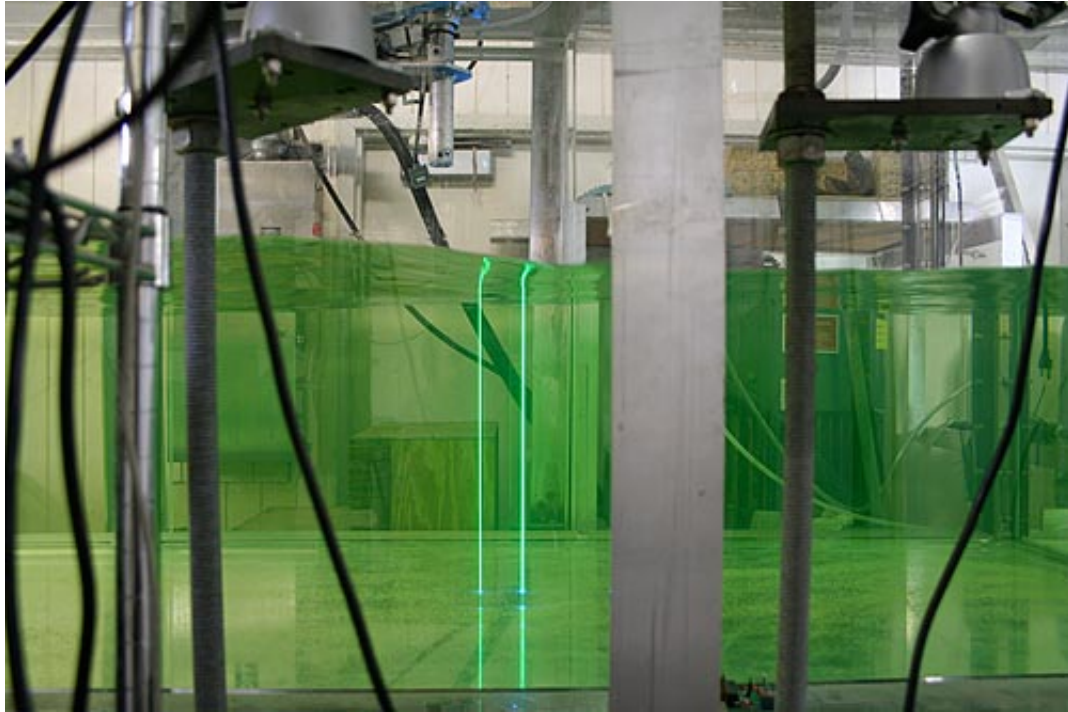


**Figure 6.4:** A photograph of laser beam in ASIST. A visible water line is brightened by the laser beam which is shot from bottom of the tank.

Next to each of the recording locations a mounted high speed camera scans the brightened vertical water line at a frequency of 547 Hz. Each frame of the camera recording snaps a grayscale picture of the vertical line of the laser beam through the tank. Because the upper part of the line is filled with air and therefore the corresponding pixels in the grayscale picture are relatively dark, and the lower part of the line is colored water illuminated by the laser therefore its pixels are rather bright. The intensity of a pixel is expressed by the numerical range between 0 to 255, where 0 means black (total absence) and 255 means white (total presence). The border line distinguished by the maximum intensity difference of neighbouring pixels, also the threshold between the dark and bright parts, indicates the

water surface. And the number of pixels from the border line down to the tank bottom (number of the bright pixels) is linearly proportional to the dynamic water depth, which is used to compute the surface elevation after calibration. Since the measurements are based on the pixel intensity, we shut off any other light sources in the wave tank chamber except the laser illuminators. The recording procedure includes two phases. In the first phase wave maker runs for 5 hours and the cameras keep recording at the same time. The second phase is a calibration process: When the water surface becomes still after the wave maker has been shut down for a while, we slowly drain the water out of the wave tank at a constant speed over a long time period until the wave tank is completely empty. During this phase the laser illuminators and cameras operate the same way as before, after the draining is done, we obtain a linear gradient of the decreasing number of the bright pixels over time, which, together with the water depth change over time, yields a linear equation that converts the camera recordings to surface elevations during the experiment.

Regarding the GF surface response, we originally planned to emulate impulse excitation by dropping an object at one of the recording locations and measuring at the other. However, due to practical reasons and lack of appropriate instruments, we decide to compare the cross-correlation result with the simulated GF response to evaluate the effectiveness of the retrieval. This is one major reason why we keep the consistency of the parameters between simulation and experiment.

### 6.3 Data analysis

The calibrated wave heights data has the same sampling frequency (547 Hz) as the cameras', which is significantly higher than what we need. Therefore we resample the converted surface elevation data at 50 Hz to simplify data analysis. Fig.6.5 is a plot of the resampled surface displacements. As one may notice, the surface elevation amplitudes have a gradually decreasing envelope during the experiment. We are not sure of the causes for this behavior; however, since phase accuracy is relatively more important than amplitude accuracy (as Roux and Fink[34] pointed out) and both the recordings have the same amplitude decreasing behavior, we don't consider the data less valuable.

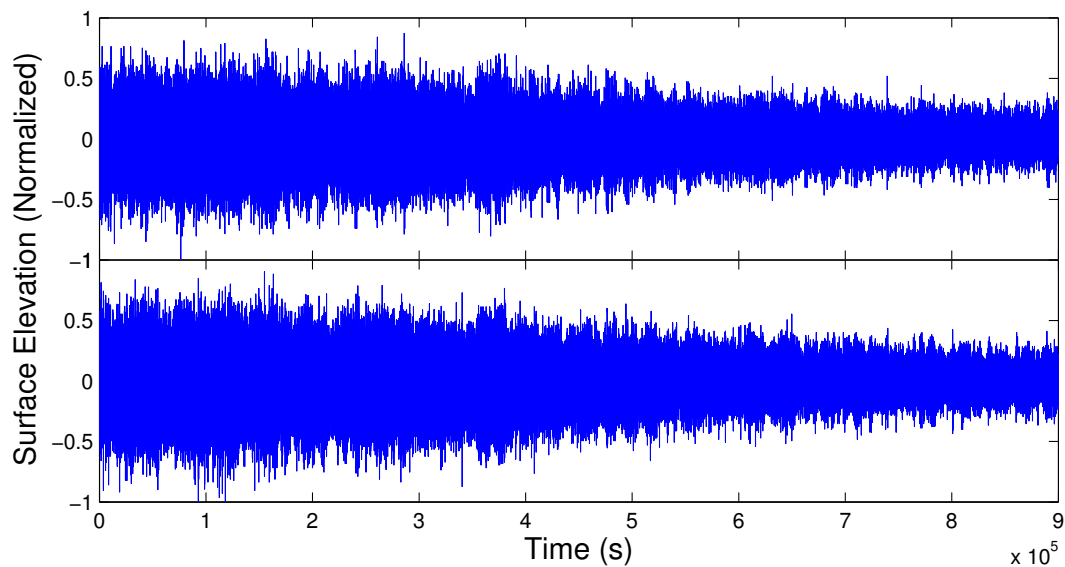


**Figure 6.5:** 5 hour time series of the surface elevation  $\eta(\mathbf{x}_A, t)$  (upper panel) and  $\eta(\mathbf{x}_B, t)$  (lower panel) measured in the wave tank. Both curves are normalized to have a maximum value of 1.

The wave tank setup, frequency range as well as peak frequency are exactly the same as those in the closed system simulation, so we could reuse the same data analysis method to process the experiment data and compare the cross-correlation result with the simulated GF response, as shown in Fig.6.6. This comparison yields a correlation coefficient of 0.62, which has 36% performance drop compared to the simulation's correlation coefficient (0.99).

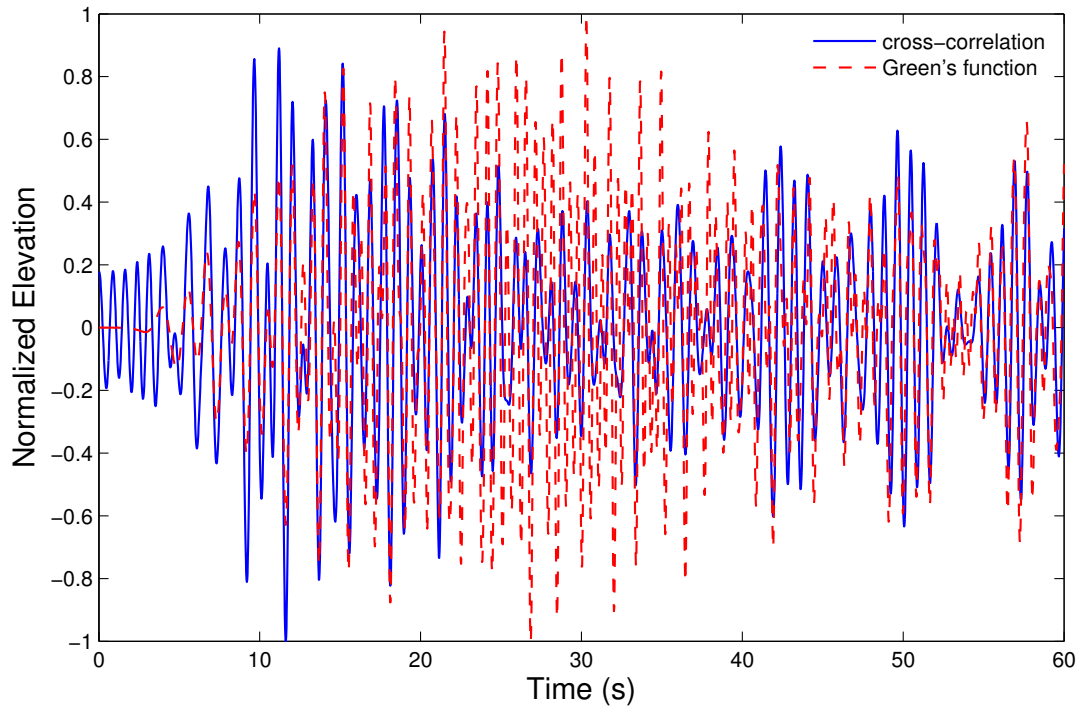


**Figure 6.6:** Cross-correlation  $(C_{AB}(t) + C_{AB}(-t))/2$  (blue curve) of random surface elevations  $\eta(\mathbf{x}_A, t)$  and  $\eta(\mathbf{x}_B, t)$  measured in the wave tank, compared to  $D(t) * G_{\eta}(\mathbf{x}_B|\mathbf{x}_A, t)$ . Cross-correlation is averaged over 240 realizations. Both curves are normalized to have a maximum absolute amplitude of 1.

It is obvious that the above estimation of GF response is far from accurate. Before a conclusion is made based on the above metric, we need to confirm that the cross-correlation result is compared with the right GF response by inspecting the surface elevation spectrum

at the two recording locations. Fig.6.7 plots the power density spectrum of the surface elevation at both recording locations.

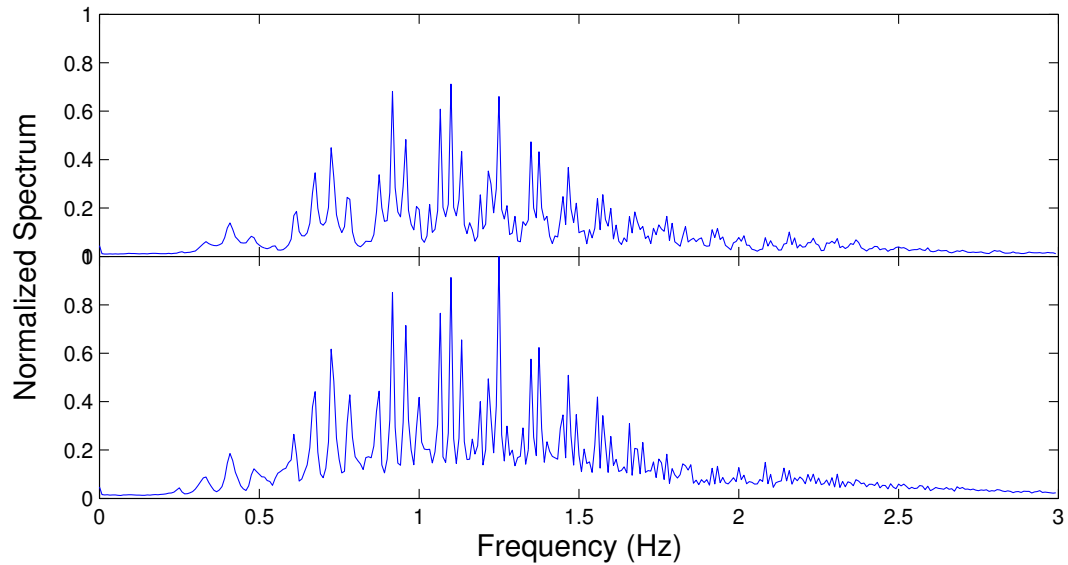


**Figure 6.7:** Power spectral density of 5 hour time series of the surface elevation  $\eta(\mathbf{x}_A, t)$  (upper panel) and  $\eta(\mathbf{x}_B, t)$  (lower panel) measured in the wave tank. The spectra are normalized by their maximum values.

The two spectral curves have some minor differences but overall they match very well. This is expected because in our experiment  $L - \mathbf{x}_B = \mathbf{x}_A$ , i.e.,  $\mathbf{x}_A$  and  $\mathbf{x}_B$  were equidistant from the ends of the tank. Now we compare the averaged spectrum (of the spectra at the two locations) with the weighting function  $\bar{d}(\omega)$  (Eq.4.14) which was applied to the original digital signal fed to the wave maker, which is shown in Fig.6.8. It is clear that the actual spectrum does not resemble the intended weighting curve. This indicates that the simulated reference GF response is not reflecting the correct energy distribution in the experiment. And this mismatch can be attributed to the transfer function that transfers the wave maker's input voltage signal to surface elevations in the wave tank. Unfortunately this transfer

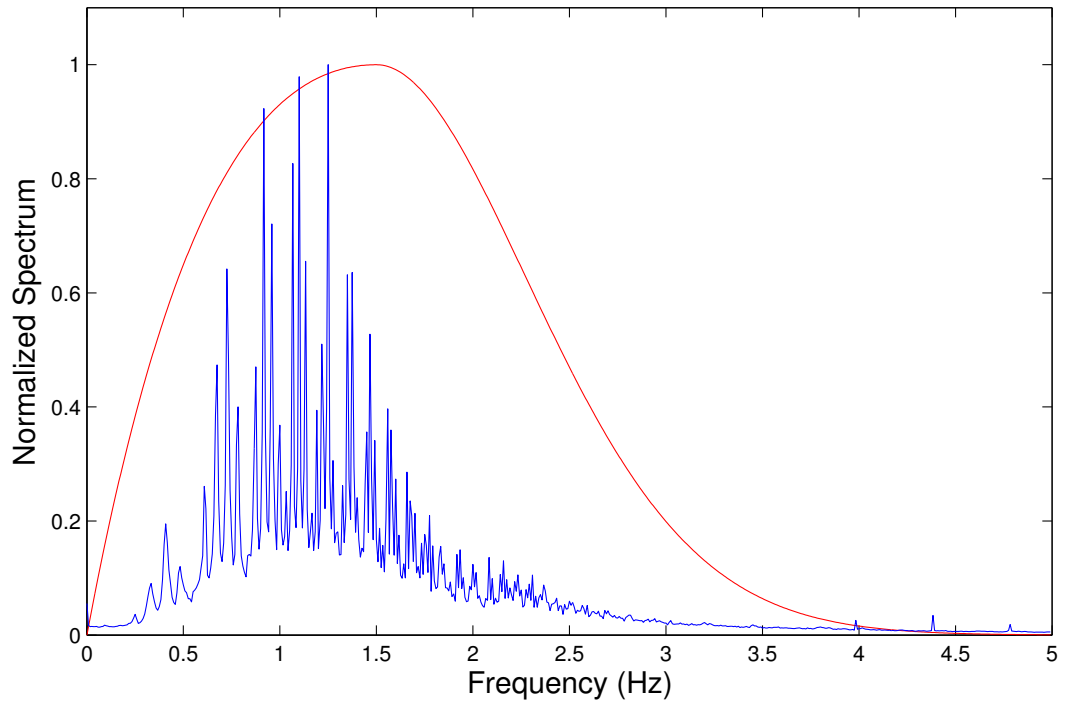


**Figure 6.8:** Averaged power density spectrum (blue curve) of 5 hours of time series of the surface elevations  $\eta(\mathbf{x}_A, t)$  and  $\eta(\mathbf{x}_B, t)$ , compared to the weighting function  $\bar{d}(\omega)$  (red curve). Both curves are normalized have a maximum value of 1.

function is not known to us, so we decide to estimate a correct weighting function  $\bar{d}(\omega)$  via an empirical approach. By curve-fitting the spectrum of the surface displacements at  $A$ , we manage to obtain a new weighting function  $\bar{d}(\omega)$  so that the product  $\bar{d}(\omega)|\cos(l\pi x_A/L_x)$  resembles the spectrum of the surface displacements at  $A$ , as shown in Fig.6.9.

Now with the new weighting function  $\bar{d}(\omega)$ , we re-simulate the reference GF response and plot it again with the cross-correlation result (as shown in Fig.6.10 and Fig.6.11). Fig.6.10 is a comparison between the newly simulated reference GF response and the cross-correlation result, and for better illustration purpose Fig.6.11 is the one-sided plot of the newly simulated reference GF response and the averaged cross-correlation result. This comparison now yields a correlation coefficient of 0.93.

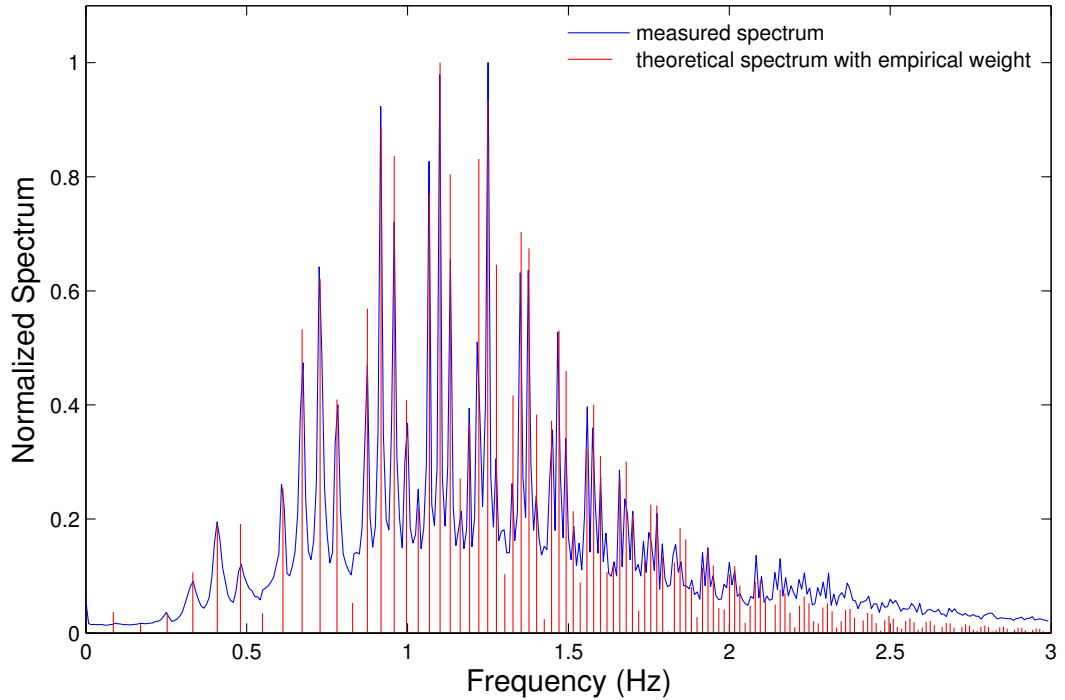


**Figure 6.9:** Theoretical spectrum with empirical weight  $\bar{d}(\omega) |\cos(l\pi x_A/L_x)|$  (red vertical bars) at  $\omega = \omega_l$ , compared to the averaged spectrum  $(|\bar{\eta}(\mathbf{x}_A, \omega)| + |\bar{\eta}(\mathbf{x}_B, \omega)|)/2$  (blue curve) in the wave tank. Both curves are normalized to have a maximum value of 1.

Recall that in Chapter 4, we showed that the numerical simulation in the wave tank yields a very good match (with a correlation coefficient of 0.99) between the averaged cross-correlation result and the simulated reference GF response. Originally we planned to compare the experiment cross-correlation result against the simulated reference GF response to evaluate the retrieval performance because the experiment in the wave tank has exactly same geometry and energy distribution as the simulation. Now since we have changed  $\bar{d}(\omega)$  to reflected the conditions in the experiment, it is reasonable to question how this modification affects the simulation result. We expect the simulation result is not affected because the modification only changes the energy distribution in frequency domain and therefore will merely reshape the reference GF response. As a matter of fact, a

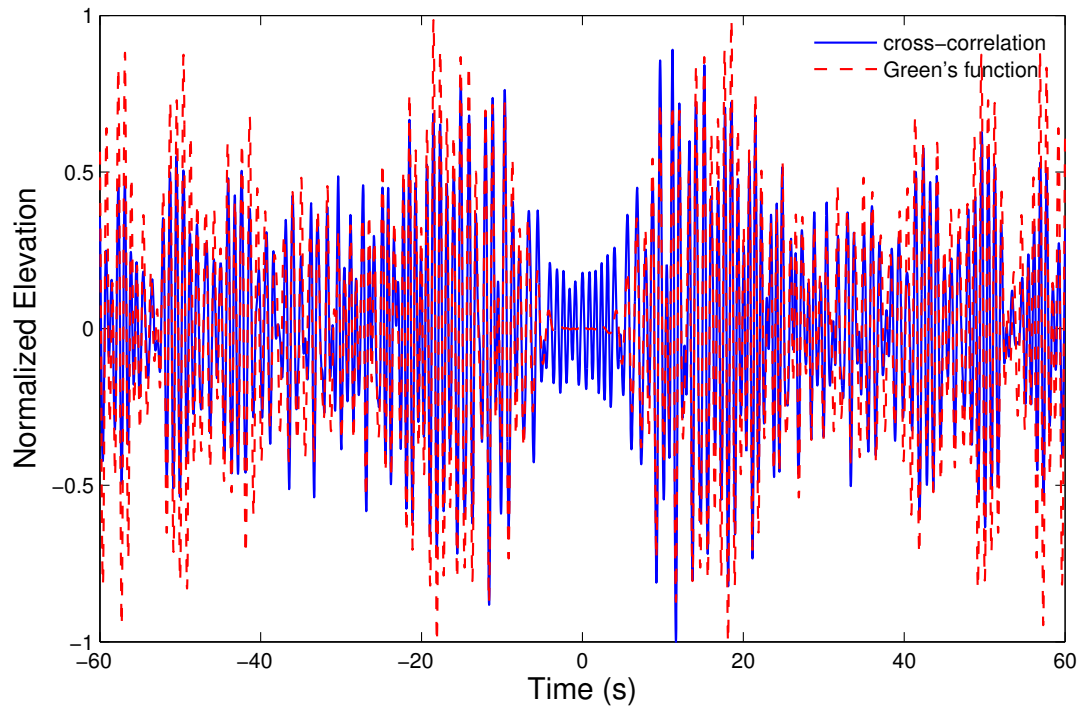


**Figure 6.10:** Cross-correlation ( $C_{AB}(t)$ ) (blue curve) of random surface elevations  $\eta(\mathbf{x}_A, t)$  and  $\eta(\mathbf{x}_B, t)$  measured in the wave tank, compared to  $D(t) * G_{\eta}(\mathbf{x}_B|\mathbf{x}_A, t)$  with empirical weight (red curve). The cross-correlation is averaged over 240 realizations. Both curves are normalized to have a maximum absolute value of 1.

simple rerun of the simulation with the empirical weighting applied indeed yields the same correlation coefficient as the previous simulation. Although the comparison result from the experiment is not as good as that in the simulation, it is actually a very high level of resemblance considering the inevitable errors that may happen in experiment procedures.

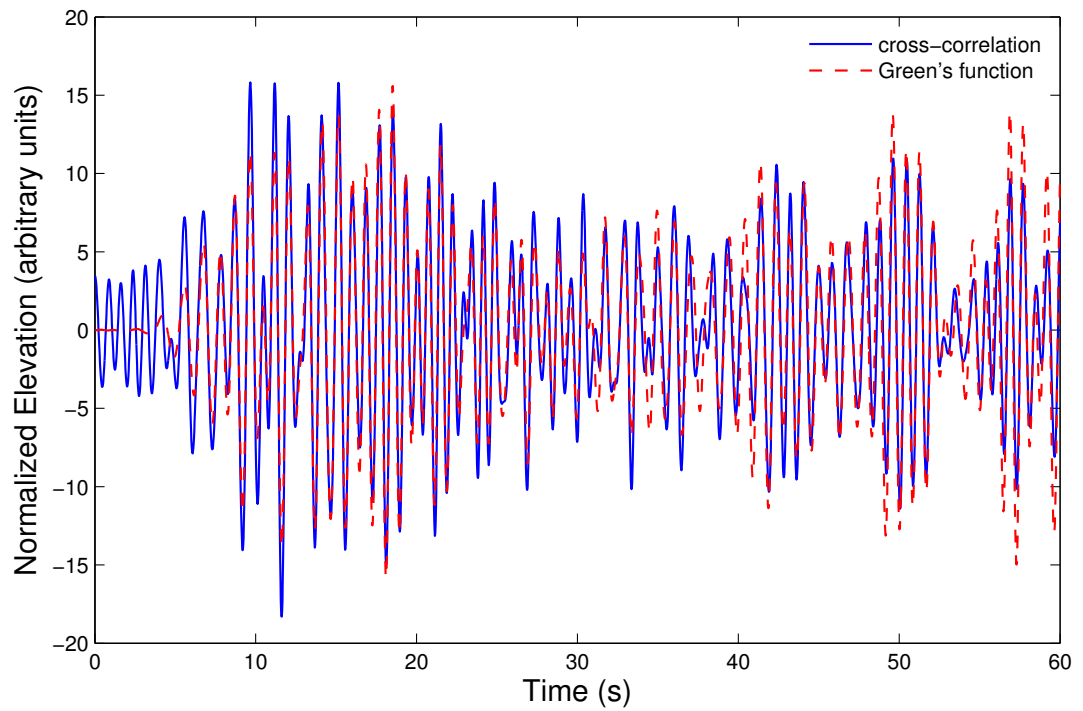


**Figure 6.11:** Cross-correlation  $(C_{AB}(t) + C_{AB}(-t))/2$  (blue curve) of random surface elevations  $\eta(\mathbf{x}_A, t)$  and  $\eta(\mathbf{x}_B, t)$  measured in the wave tank, compared to  $D(t) * G_\eta(\mathbf{x}_B|\mathbf{x}_A, t)$  with empirical weight (red curve). The cross-correlation is averaged over 240 realizations. Both curves are normalized to have the same total energy between 3 and 60 s.

# Chapter 7

## Conclusion and Discussion

In this thesis work, we first introduced the concept and value of GF and GF retrieval in Chapter 1. Then in Chapter 2 we reviewed some previous research works regarding GF retrieval using cross-correlation in various fields, especially in ocean acoustics and seismology, which encouraged our interests of the applicability of a similar approach in a random water wave field. After that in Chapter 3 we went through theoretical derivations to prove that under linear water wave theory GF can be extracted by cross-correlating random water wave elevations. The theoretical derivations were presented in two different environments, namely an open system and a closed system. Following the theoretical proof, Chapter 4 presents numerical simulations with both open and closed systems to support the theoretical proof. Then in Chapter 5 we explored the theory with water wave surface elevation data from two field experiments. With Chapter 5 being our attempt in an actual open field, we also conducted an indoor wave tank experiment to provide insights regarding the closed system, which is covered by Chapter 6.

Both the open system and closed system simulations yield good agreements with the theoretical predictions. In the open system simulation we created a random water wave field by exciting randomly distributed impulse sources in a circular domain, at time instances that are also randomly selected during a period of time. The superposition of all waves of different amplitudes propagating in all directions creates an ideal random wave field, where equipartition is established. In the closed system simulation, we took a different approach in creating the random wave field by exciting each mode within the limited bandwidth along the wave tank direction. Surface waves were simulated to only propagate along the tank direction because the tank geometry is narrow across the tank and previous study had showed that cross-correlation result is mainly contributed by waves that propagate along the receiver axis (which is also along the tank) and a global equipartition requirement is not necessary. While the geometries and approaches are different, the two simulations both yield high correlation coefficients and successfully demonstrate the feasibility of GF estimation using cross-correlation. The wave tank experiment was done to remake the closed system simulation in a actual wave tank with the exact same geometry. After fixing the energy distribution issue the estimated GF using the wave tank data agrees very well with the simulated reference GF response. For the open system, we cautiously analyzed the field experiments data with various known issues and tried to avoid local wind effects based on their wind speed measurements during the experiments. However, the measurements from these fields experiments failed to produce a deterministic GF response.

The failure with the attempt to extract deterministic GF response from the field experiment data could directly relate to how the data was collected. The technique of retrieving GF from a random wave field relies highly on the phase coherence, which could be easily lost with the already mentioned various issues in Chapter 5. The constant measurement gaps that exist in both the field experiments make it impossible to obtain an accurate long time record of the actual surface elevations. All of the instruments used to measure surface displacements were essentially moored buoys loaded with equipment. Although these buoys were moored, they drift horizontally along with currents for certain distances. Therefore, instead of measuring the surface elevations at one fixed location, it in fact measured at multiple locations in a relatively fixed region. Such measurements very likely caused loss of phase coherence at certain frequencies. In SW06 experiment the ASIS buoys are expected to drift up to 90 m horizontally relative to their mean positions, the relative drift between those two buoys should be much smaller, but rather hard to estimate. The surface elevation spectrum has a peak frequency of 0.35 Hz, which corresponds to a wavelength of about 12 m. It is likely that the relative drift distance between Romeo and Yankee is close to or larger than this wavelength during the time window we chose, so that phase coherence was lost between the buoys around the peak frequency. Because of the strict requirement of coherent phases between measuring instruments, it is necessary to only use measurements that is collected by equipment on fixed platforms for the purpose of GF retrieval with random water waves.

Another possible factor that could lead to the failure of estimating GF response with the field experiment measurements is the local wind effect. FECTCH was deliberately designed to study air-sea interactions and wave growth caused by winds, the time frame of the experiment was especially chosen to observe seasonal high wind phenomenons. SW06 was aimed to study underwater acoustics, but the measurements of surface elevations were also intended for air-sea interaction research in the first place. Besides, the long distance between the ASIS buoys made it very easy for local winds to alter wave phases. We tried to minimize the wind effects by only correlating a portion of the field measurements where wind speed was low, but it is still highly possible that local wave generation and dissipation played significant roles at the measuring locations.

Finally, if we pay less attention on issues with the field experiment data, we could give another possible explanation for the unsuccessful attempt of GF retrieval using the field experiment data by questioning the underlying theory. As stated many times throughout this thesis, the technique of estimating GF response via cross-correlation is established on the foundation of super-position principle, which only applies to systems governed by linear equations. And our theoretical derivation with a random water wave field is based on the approximation of linear theory, which requires  $ka$  to be small (where  $k$  is wave number and  $a$  is wave amplitude). But in reality water wave field is not linear and nonlinear effects exist. The nonlinear effects that are excluded by us in theory may make big enough difference in the actual wave field, which overshadows the effect of cross-correlation in GF estimation. The most visible nonlinear effect is the behavior of short waves traveling

faster than is predicted in linear theory due to phase locking. However, this behavior should only alter the estimated GF response but not lead to the complete failure of not producing deterministic structure at all. Therefore, it is not convincing that this could account for the failure of our work in Chapter 5. In fact a feasible way to understand the role of nonlinear effects in cross-correlation based GF retrieval is to conduct many more wave tank experiments with different  $ka$  and see how GF estimation is affected.

# Bibliography

- [1] G. D. Bensen, M. H. Ritzwoller, M. P. Barmin, A. L. Levshin, F. Lin, M. P. Moschetti, N. M. Shapiro, and Y. Yang. Processing seismic ambient noise data to obtain reliable broad-band surface wave dispersion measurements. *Geophysical Journal International*, 169(3):1239–1260, 2007.
- [2] Florent Brenguier, Nikolai M. Shapiro, Michel Campillo, Valérie Ferrazzini, Zacharie Duputel, Olivier Coutant, and Alexandre Nercessian. Towards forecasting volcanic eruptions using seismic noise. *Nature Geoscience*, 1(2):126–130, 2008.
- [3] M. G. Brown and C. Lu. Green’s function retrieval in a field of random water waves. *submitted to Wave Motion*, 2015.
- [4] Michael G. Brown. Noise interferometry in an inhomogeneous environment in the geometric limit. *The Journal of the Acoustical Society of America*, 130(4):EL173–9, 2011.
- [5] M. Campillo and A. Paul. Long-range correlations in the diffuse seismic coda. *Science*, 299(5606):547–9, 2003. Campillo, Michel Paul, Anne eng New York, N.Y. 2003/01/25 04:00 Science. 2003 Jan 24;299(5606):547-9.
- [6] Andrew Curtis, Heather Nicolson, David Halliday, Jeannot Trampert, and Brian Baptie. Virtual seismometers in the subsurface of the earth from seismic interferometry. *Nature Geoscience*, 2(10):700–704, 2009.
- [7] Arnaud Derode, Eric Larose, Michel Campillo, and Mathias Fink. How to estimate the greens function of a heterogeneous medium between two passive sensors? application to acoustic waves. *Applied Physics Letters*, 83(15):3054, 2003.
- [8] Arnaud Derode, Eric Larose, Mickael Tanter, Julien De Rosny, Arnaud Tourin, Michel Campillo, and Mathias Fink. Recovering the greens function from field-field correlations in an open scattering medium (I). *The Journal of the Acoustical Society of America*, 113(6):2973–2976, 2003.
- [9] Mark A. Donelan, Brian K. Haus, William J. Plant, and Olivier Troianowski. Modulation of short wind waves by long waves. *Journal of Geophysical Research: Oceans (1978–2012)*, 115(C10), 2010.

- [10] Deyan Draganov, Kees Wapenaar, Wim Mulder, Johannes Singer, and Arie Verdel. Retrieval of reflections from seismic background-noise measurements. *Geophysical Research Letters*, 34(4), 2007.
- [11] Deyan Draganov, Kees Wapenaar, and Jan Thorbecke. Seismic interferometry: Reconstructing the earth's reflection response. *Geophysics*, 71(4):SI61–SI70, 2006.
- [12] William M. Drennan, Hans C. Graber, Danièle Hauser, and Céline Quentin. On the wave age dependence of wind stress over pure wind seas: Fluxes, surface waves, remote sensing, and ocean circulation in the north mediterranean sea: results from the fetch experiment. *Journal of Geophysical Research*, 108(C3):FET10–1, 2003.
- [13] H. Dupuis, C. Guerin, D. Hauser, A. Weill, P. Nacass, W.M. Drennan, S. Cloché, and H.C. Graber. Impact of flow distortion corrections on turbulent fluxes estimated by the inertial dissipation method during the fetch experiment on r/v l'atalante. *Journal of Geophysical Research: Oceans (1978–2012)*, 108(C3), 2003.
- [14] T.L. Duvall, S.M. Jefferies, J.W. Harvey, and M.A. Pomerantz. Time-distance helioseismology. *Nature*, 362(6419):430–432, 1993.
- [15] Edward Field and Klaus Jacob. The theoretical response of sedimentary layers to ambient seismic noise. *Geophysical Research Letters*, 20(24):2925–2928, 1993.
- [16] J.T. Fricke, L.G. Evers, P.S.M. Smets, K. Wapenaar, and D.G. Simons. Infrasonic interferometry applied to microbaroms observed at the large aperture infrasound array in the netherlands. *Journal of Geophysical Research: Atmospheres*, 119(16):9654–9665, 2014.
- [17] Oleg Godin. Recovering the acoustic greens function from ambient noise cross correlation in an inhomogeneous moving medium. *Physical Review Letters*, 97(5), 2006.
- [18] Oleg A. Godin. Cross-correlation function of acoustic fields generated by random high-frequency sources. *The Journal of the Acoustical Society of America*, 128(2):600–610, 2010.
- [19] Oleg A. Godin, Vladimir G. Irisov, and Mikhail I. Charnotskii. Passive acoustic measurements of wind velocity and sound speed in air. *The Journal of the Acoustical Society of America*, 135(2):EL68–EL74, 2014.
- [20] Oleg A. Godin, Nikolay A. Zabortin, Anne F. Sheehan, and John A. Collins. Interferometry of infragravity waves off new zealand. *Journal of Geophysical Research: Oceans*, 119(2):1103–1122, 2014.

- [21] Matthew M. Haney. Infrasonic ambient noise interferometry from correlations of microbaroms. *Geophysical Research Letters*, 36(19), 2009.
- [22] Nicholas Harmon, Timothy Henstock, Meric Srokosz, Frederik Tilmann, Andreas Rietbrock, and Penny Barton. Infragravity wave source regions determined from ambient noise correlation. *Geophysical Research Letters*, 39(4), 2012.
- [23] D. Hauser. The fetch experiment: An overview. *Journal of Geophysical Research*, 108(C3), 2003.
- [24] Simon King and Andrew Curtis. Suppressing nonphysical reflections in greens function estimates using source-receiver interferometry. *Geophysics*, 77(1):Q15–Q25, 2012.
- [25] Fan-Chi Lin, Morgan P. Moschetti, and Michael H. Ritzwoller. Surface wave tomography of the western united states from ambient seismic noise: Rayleigh and love wave phase velocity maps. *Geophysical Journal International*, 173(1):281–298, 2008.
- [26] Oleg I. Lobkis and Richard L. Weaver. On the emergence of the greens function in the correlations of a diffuse field. *The Journal of the Acoustical Society of America*, 110(6):3011, 2001.
- [27] James Lynch and Dajun Tang. Overview of shallow water 2006 jasa el special issue papers. *The Journal of the Acoustical Society of America*, 124(3):EL63–EL65, 2008.
- [28] Y.A. Melnikov, J.A. Melnykov, and M.Y. Melnikov. *Green's Functions: Construction and Applications*. De Gruyter studies in mathematics. De Gruyter, 2012.
- [29] Arthur E. Newhall, Timothy F. Duda, Keith von der Heydt, James D. Irish, John N. Kemp, Steven A. Lerner, Stephen P. Liberatore, Ying-Tsong Lin, James F. Lynch, and Andrew R. Maffei. Acoustic and oceanographic observations and configuration information for the whoi moorings from the sw06 experiment. Technical report, DTIC Document, 2007.
- [30] Heidi Pettersson. Directional wave measurements from three wave sensors during the fetch experiment. *Journal of Geophysical Research*, 108(C3), 2003.
- [31] Rafael J. Ramos, Björn Lund, and Hans C. Graber. Determination of internal wave properties from x-band radar observations. *Ocean Engineering*, 36(14):1039–1047, 2009.
- [32] James Rickett and Jon Claerbout. Acoustic daylight imaging via spectral factorization: Helioseismology and reservoir monitoring. *The Leading Edge*, 18:957, 1999.

- [33] J.E. Rickett and J.F. Claerbout. Calculation of the sun's acoustic impulse response by multi-dimensional spectral factorization. *Solar Physics*, 192(1-2):203–210, 2000.
- [34] Philippe Roux and Mathias Fink. Greens function estimation using secondary sources in a shallow water environment. *The Journal of the Acoustical Society of America*, 113(3):1406, 2003.
- [35] Philippe Roux, W. A. Kuperman, and Npal Group the. Extracting coherent wave fronts from acoustic ambient noise in the ocean. *The Journal of the Acoustical Society of America*, 116(4):1995, 2004.
- [36] Philippe Roux, Karim G. Sabra, W. A. Kuperman, and Andre Roux. Ambient noise cross correlation in free space: Theoretical approach. *The Journal of the Acoustical Society of America*, 117(1):79, 2005.
- [37] RSMAS. Asist. <http://www.rsmas.miami.edu/assets/images/asist/tank-from-inside.jpg>. [Online; accessed 29-April-2015].
- [38] RSMAS. Asist. [http://www.rsmas.miami.edu/assets/images/asist/IMG\\_3699.jpg](http://www.rsmas.miami.edu/assets/images/asist/IMG_3699.jpg). [Online; accessed 29-April-2015].
- [39] S. M. Rytov. On thermal agitation in distributed systems. *Soviet Physics Doklady*, 1:555–559, May 1956.
- [40] Sergej M. Rytov, Yurii A. Kravtsov, and Valeryan I. Tatarskii. *Principles of statistical radiophysics 3*. Springer New York Inc., New York, NY, 1989.
- [41] Karim G. Sabra. Extracting time-domain green's function estimates from ambient seismic noise. *Geophysical Research Letters*, 32(3), 2005.
- [42] Karim G. Sabra, Philippe Roux, and W. A. Kuperman. Arrival-time structure of the time-averaged ambient noise cross-correlation function in an oceanic waveguide. *The Journal of the Acoustical Society of America*, 117(1):164, 2005.
- [43] Francisco J. Sánchez-Sesma and Michel Campillo. Retrieval of the greens function from cross correlation: the canonical elastic problem. *Bulletin of the Seismological Society of America*, 96(3):1182–1191, 2006.
- [44] N. M. Shapiro. Emergence of broadband rayleigh waves from correlations of the ambient seismic noise. *Geophysical Research Letters*, 31(7), 2004.
- [45] N. M. Shapiro, M. Campillo, L. Stehly, and M. H. Ritzwoller. High-resolution surface-wave tomography from ambient seismic noise. *Science*, 307(5715):1615–8, 2005. Shapiro, Nikolai M Campillo, Michel Stehly, Laurent Ritzwoller, Michael H eng New York, N.Y. 2005/03/12 09:00 Science. 2005 Mar 11;307(5715):1615-8.

- [46] Nikolai M. Shapiro, Michel Campillo, Laurent Stehly, and Michael H. Ritzwoller. High-resolution surface-wave tomography from ambient seismic noise. *Science*, 307(5715):1615–1618, 2005.
- [47] Evert Slob, Deyan Draganov, and Kees Wapenaar. Interferometric electromagnetic green's functions representations using propagation invariants. *Geophysical Journal International*, 169(1):60–80, 2007.
- [48] Evert Slob and Kees Wapenaar. Electromagnetic green's functions retrieval by cross-correlation and cross-convolution in media with losses. *Geophysical Research Letters*, 34(5), 2007.
- [49] Roel Snieder. Extracting the greens function from the correlation of coda waves: A derivation based on stationary phase. *Physical Review E*, 69(4), 2004.
- [50] Roel Snieder. Extracting the greens function of attenuating heterogeneous acoustic media from uncorrelated waves. *The Journal of the Acoustical Society of America*, 121(5):2637–2643, 2007.
- [51] Roel Snieder and Kees Wapenaar. Imaging with ambient noise. *Physics Today*, 63(9):44, 2010.
- [52] Roel Snieder, Kees Wapenaar, and Ulrich Wegler. Unified greens function retrieval by cross-correlation; connection with energy principles. *Physical Review E*, 75(3):036103, 2007.
- [53] L. Stehly, Michel Campillo, B. Froment, and R.L. Weaver. Reconstructing green's function by correlation of the coda of the correlation (c3) of ambient seismic noise. *Journal of Geophysical Research: Solid Earth (1978–2012)*, 113(B11), 2008.
- [54] L. Stehly, Michel Campillo, and N.M. Shapiro. A study of the seismic noise from its long-range correlation properties. *Journal of Geophysical Research: Solid Earth (1978–2012)*, 111(B10), 2006.
- [55] Dajun Tang, James N. Moum, James F. Lynch, Phil Abbot, Ross Chapman, Peter H. Dahl, Timothy F. Duda, Glen Gawarkiewicz, Scott Glenn, John A. Goff, Hans Graber, John Kemp, Andrew Maffei, Jonathan D. Nash, and Arthur Newhall. Shallow water '06: A joint acoustic propagation/nonlinear internal wave physics experiment. *Oceanography*, 20(4):156–167, 2007.
- [56] Kees Wapenaar. Retrieving the elastodynamic green's function of an arbitrary inhomogeneous medium by cross correlation. *Physical Review Letters*, 93(25):254301, 2004.

- [57] Kees Wapenaar, Deyan Draganov, Johan O.A. Robertsson, and SEG Geophysics Reprint Series No. Seismic interferometry: History and present status. *LEADING EDGE*, 25:1082–1092, 2007.
- [58] Kees Wapenaar and Jacob Fokkema. Greens function representations for seismic interferometry. *Geophysics*, 71(4):SI33–SI46, 2006.
- [59] Richard L. Weaver. Equipartition and mean-square responses in large undamped structures. *The Journal of the Acoustical Society of America*, 110(2):894, 2001.
- [60] Richard L. Weaver and Oleg I. Lobkis. Diffuse fields in open systems and the emergence of the greens function (I). *The Journal of the Acoustical Society of America*, 116(5):2731, 2004.
- [61] Ulrich Wegler and C. Sens-Schönfelder. Fault zone monitoring with passive image interferometry. *Geophysical Journal International*, 168(3):1029–1033, 2007.
- [62] Simon C. Woods and Alan H. Greenaway. Wave-front sensing by use of a greens function solution to the intensity transport equation. *JOSA A*, 20(3):508–512, 2003.
- [63] Sihua Zheng, Xinlei Sun, Xiaodong Song, Yingjie Yang, and Michael H. Ritzwoller. Surface wave tomography of china from ambient seismic noise correlation. *Geochemistry, Geophysics, Geosystems*, 9(5), 2008.